This is a pre-copyedited, author-produced version of an article accepted for publication, following peer review.

[Article begins on next page]

1

Decoupling of particles and dissolved iron downstream of Greenlandic

glacier outflows

4

C. M. van Genuchten[1], M. T. Rosing[2], M. J. Hopwood[3], T. Liu[3], J. Krause[3], L.

Meire[4,5]

7

[1]Department of Geochemistry, Geological Survey of Denmark and Greenland,
Copenhagen, Denmark

[2]Globe Institute, University of Copenhagen, Copenhagen Denmark

[3]GEOMAR Helmholtz Centre for Ocean Research Kiel, Kiel, Germany

[4]Greenland Climate Research Centre, Greenland Institute of Natural Resources,
Nuuk, Greenland

[5]Department of Estuarine and Delta Systems, Royal Netherlands Institute for Sea
Research, Yerseke, The Netherlands

24   Abstract

25   Glaciers can be a significant and locally dominant source of iron (Fe), a biologically

26   essential micronutrient, in high latitude coastal seas. The vast majority of this glacial Fe delivery

27   is associated with particles, yet the speciation of the solid-phase Fe and specifically the

28   relationships that govern exchange between particulate and dissolved Fe phases in these

29   environments are poorly described. In this work, we performed measurements of in situ

30   dissolved Fe (dFe) along meltwater and particle plumes in three transects around Disko Bay and

31   Ameralik Fjord (West Greenland). Measurements of dFe were combined with Fe K-edge X-ray

32   absorption spectroscopy analysis of ~40 suspended sediment samples obtained from the same

33   transects and from select depth profiles down to 300 m. We observed relatively constant dFe

34   levels (4 to 10 nM for nearly all dFe measurements) across fjords with widely varying particulate

35   Fe(II) contents (from 20 to 90% Fe(II)), indicating that dFe concentrations had little dependence

36   on the oxidation state of Fe in the suspended sediment. Particulate Fe data were grouped by

37   underlying bedrock geology, with suspended sediment consisting of 80-90% biotite-like Fe(II) in

38   fjords with Precambrian shield geology and poorly-ordered Fe(III) particles (<20-30% Fe(II)) in

39   one fjord with suspended sediments derived from tertiary basalts. Our characterization data

40   indicated no significant change in the average Fe oxidation state and bonding environment of

41   particles along the fjord transects, implying that Fe(II) in biotite-like coordination is not a readily

42   labile Fe form on this spatial scale. Our results suggest that dFe in these glacially-modified

43   coastal waters is buffered at a relatively constant low nM concentration due to factors other than

44   particle Fe mineralogy and that glacier-derived Fe phases are relatively inert on this spatial scale.

45

46   Keywords: Fe speciation; suspended sediment; X-ray absorption spectroscopy; glacial meltwater

2

1. Introduction

Iron (Fe) is an essential micronutrient for marine primary production. The poor solubility of Fe in seawater results in sub- or low nM concentrations of dissolved Fe (dFe), the most bioavailable Fe form, throughout most of the ocean (Kuma and Matsunaga, 1995; Schlitzer et al., 2018). Because of this low solubility, Fe availability limits or co-limits phytoplankton growth across large areas of the open ocean (Martin et al., 1991; Tagliabue et al., 2017), and thus plays a regulatory role in the global biological carbon pump, affecting atmospheric CO_2 concentrations and thereby global climate. The role of Fe in limiting marine primary production is especially pronounced in regions of the high latitude offshore ocean that receive minimal inputs of aeolian dust, which is the primary source of 'new' Fe into the offshore ocean (Fan et al., 2006). An additional Fe source to the high latitude ocean is glacial meltwater (Statham et al., 2008). This Fe source is particularly relevant to fjords and coastal regions surrounding the Greenland Ice Sheet (GrIS), which discharges ~1200 Gt of freshwater annually to surrounding waters (Bamber et al., 2018). The meltwater discharged from the GrIS can contain substantial loads (>3000 mg/L) of fine-grained glacially abraded particles that are rich in Fe and other biologically relevant elements including silicon (Si) (Meire et al., 2016; Sukstorf et al., 2020). Due to unabated warming Arctic air temperatures and intensified GrIS melting, fluxes of any glacially-derived elements that scale with discharge volume are expected to increase in the future (Vizcaíno et al., 2014).

Meltwater discharge around Greenland is known to release large quantities of Fe into adjacent coastal waters, with the vast majority of this Fe contained in suspended particles (Hawkings et al., 2014; Kanna et al., 2020). However, the solid-phase Fe speciation in glacier outflows and especially the relationships that govern exchange between particulate and dissolved

70 Fe phases are poorly understood (Ardiningsih et al., 2020; Lippiatt et al., 2010). Knowledge of

71 particulate Fe speciation is thought to be critical because key properties of solid-phase Fe,

72 including solubility and bioavailability, can vary widely with oxidation state and bonding

73 environment (Matsunaga et al., 1995). For example, Fe(III)-bearing solids are less soluble and

74 more thermodynamically stable in the euphotic zone than their Fe(II)-rich counterparts, which

75 may lead to lower dFe availability in areas where Fe(III)-bearing suspended sediment dominate

76 (Von Der Heyden et al., 2012). Of the possible Fe(III)-bearing minerals, poorly-ordered Fe(III)

77 (oxyhydr)oxide, herein referred to as hydrous ferric oxide (HFO), has been suggested as a key Fe

78 host phase in glacial meltwater due to its expected prevalence and potential bioavailability

79 (Bhatia et al., 2013; Raiswell, 2011; Raiswell et al., 2006). While many studies invoke nanoscale

80 Fe(III) precipitates as critical Fe sources to biota in glaciated systems, the importance of Fe(II)-

81 bearing minerals is also gaining attention. Recently, solids containing up to 40% particulate

82 Fe(II) were reported in Leverett Glacier (West Greenland) sediments, prompting speculation that

83 the GrIS can be a source of bioaccessible particulate Fe(II) to the ocean (Hawkings et al., 2018),

84 although whether this measurably increases Fe availability to biota, and via what mechanisms,

85 has not been extensively quantified (Shoenfelt et al., 2017). Large supplies of Fe(II)-bearing

86 sediment in meltwater may have important implications because 1) Fe(II)-rich aerosol particles

87 have been showed to enhance phytoplankton growth more than Fe(III)-bearing particles, 2)

88 particulate Fe(II) is generally more soluble than Fe(III), which may favour dFe release and 3)

89 there is some limited evidence of direct surface Fe acquisition from Fe(II)-rich particles by

90 diatoms (Shoenfelt et al., 2017). Taken together, these previous studies provide a theoretical

91 basis for investigating the potentially diverse effects of ferrous and ferric particles on dFe

92 availability around Greenland.

4

93   Only few studies have investigated particulate Fe and dFe behaviour concurrently in such

94   regions, and of these investigations, indirect measurements of Fe mineralogy (i.e., chemical

95   extractions) are most common (Raiswell et al., 2010). However, the use of chemical extractions,

96   which are based on the reaction of (in)organic acids with solids, to characterize particulate Fe has

97   several disadvantages. First, poorly-ordered HFO rarely occurs in the environment without

98   impurities, such as Si and Al, which can exceed 30 mol% (Adra et al., 2013; Carlson and

99   Schwertmann, 1981). Since the structure and reactivity (i.e., transformation rates, sorption

100   properties) of impurity-rich HFO differ from pure, lab-synthesized 2-line ferrihydrite (2LFh)

101   (Kraal et al., 2019), extractions calibrated to pure 2LFh can incorrectly estimate poorly-ordered

102   and potentially bioavailable Fe in sediments. Second, key extraction parameters, including time,

103   pH and extractant type and concentration, vary widely across studies (Conway et al., 2015;

104   Raiswell et al., 2016), which complicates the comparison of independent datasets. In contrast to

105   indirect methods of identifying Fe mineralogy, direct measurement of the Fe coordination

106   environment using X-ray absorption spectroscopy (XAS) is less prone to ambiguous

107   determination of particulate Fe speciation and XAS data can be compared easily with large

108   spectra databases to aid interpretation (Kelly et al., 2008). Combined with dFe measurements,

109   the information obtained from XAS data can provide new insights into the coupling of solid-

110   phase Fe and dFe.

111   The objective of this work was to determine particulate Fe speciation in parallel with in

112   situ dFe concentrations in areas receiving large volumes of GrIS meltwater in order to investigate

113   the coupling of particulate speciation and dFe availability in fjords with contrasting suspended

114   sediment Fe mineralogy. To this end, we measured dFe in fjord surface water samples collected

115   from three transects up to 100 km in length around Disko Bay and along Ameralik Fjord (West

5

116   Greenland). In situ dFe concentrations were paired with a comprehensive set of ~40 suspended

117   sediment samples obtained from the same transects and from depth profiles down to 300 m. The

118   sediment samples were analysed by Fe K-edge XAS to identify the average oxidation state of

119   particulate Fe and resolve the host Fe phase. Our results highlight the ubiquity of Fe(II)-bearing

120   minerals in GrIS meltwater and associated fjord suspended sediments and, critically, suggest the

121   decoupling of particulate Fe speciation and dissolved Fe on this spatial scale.

122   2. Methods

123   2.1 Sampling regions

124   Three transects were performed in West Greenland (Figure 1). Two transects were

125   conducted in the Disko Bay area (Ilulissat, mid-West Greenland) using RV Sanna in July 2019.

126   The first transect was performed in Arfersiorfik Fjord, a large (>100 km) fjord located just south

127   of Kangaatsiaq in the southern part of Disko Bay and will be referred to as the Arfersiorfik (AF)

128   transect. A depth profile was also conducted in the Eqi Fjord, north of Ilulissat (Figure 1).

129   Geology of the coast of mainland Greenland along the Arfersiorfik transect and Eqi Fjord is

130   Precambrian basement dominated by amphibolite – granulite facies gneisses. Additionally, a

131   second transect herein referred to as Disko Island (DI) was conducted in the Disko Fjord, a fjord

132   of ~50 km length located in the southwest of Disko Island. Disko Island (Qeqertarsuaq) geology

133   is composed of younger tertiary basalts resting on Precambrian felsic basement (Mascarenhas

134   and Zielinski, 2019).

135   Data were also collected in Ameralik (AM) Fjord and the neighbouring Godthåbsfjord

136   (GHF) situated on the southwest coast of Greenland near the capital city of Nuuk. These fjords

137   are located in the Archaean Block of western Greenland, giving rise to a geology composed

138   primarily of Tonalite-Trondhjemite-Granodiorite gneisses (Naeraa et al., 2014). In Ameralik,

139   data were collected along a transect during two separate research cruises with RV Sanna in

140   August 2019 (fjord water) and a smaller vessel in July 2015 (suspended sediment). Although

141   data for the Ameralik transect were collected in different years, the time of the year was similar

142   and the particle geology is not likely to change substantially on this timescale. Depth-resolved

143   samples were collected from a single location in Godthåbsfjord (64°38' N, 50°09' W) near the

144   terminus of the glacier Narsap Sermia (Figure 1) in June 2015. Finally, a glacially abraded rock

7

145   flour sample was also collected directly from a dry raised seabed deposit 15 km north of Nuuk

146   (64°17' N, 51°43' W; green square in Figure 1D).

147
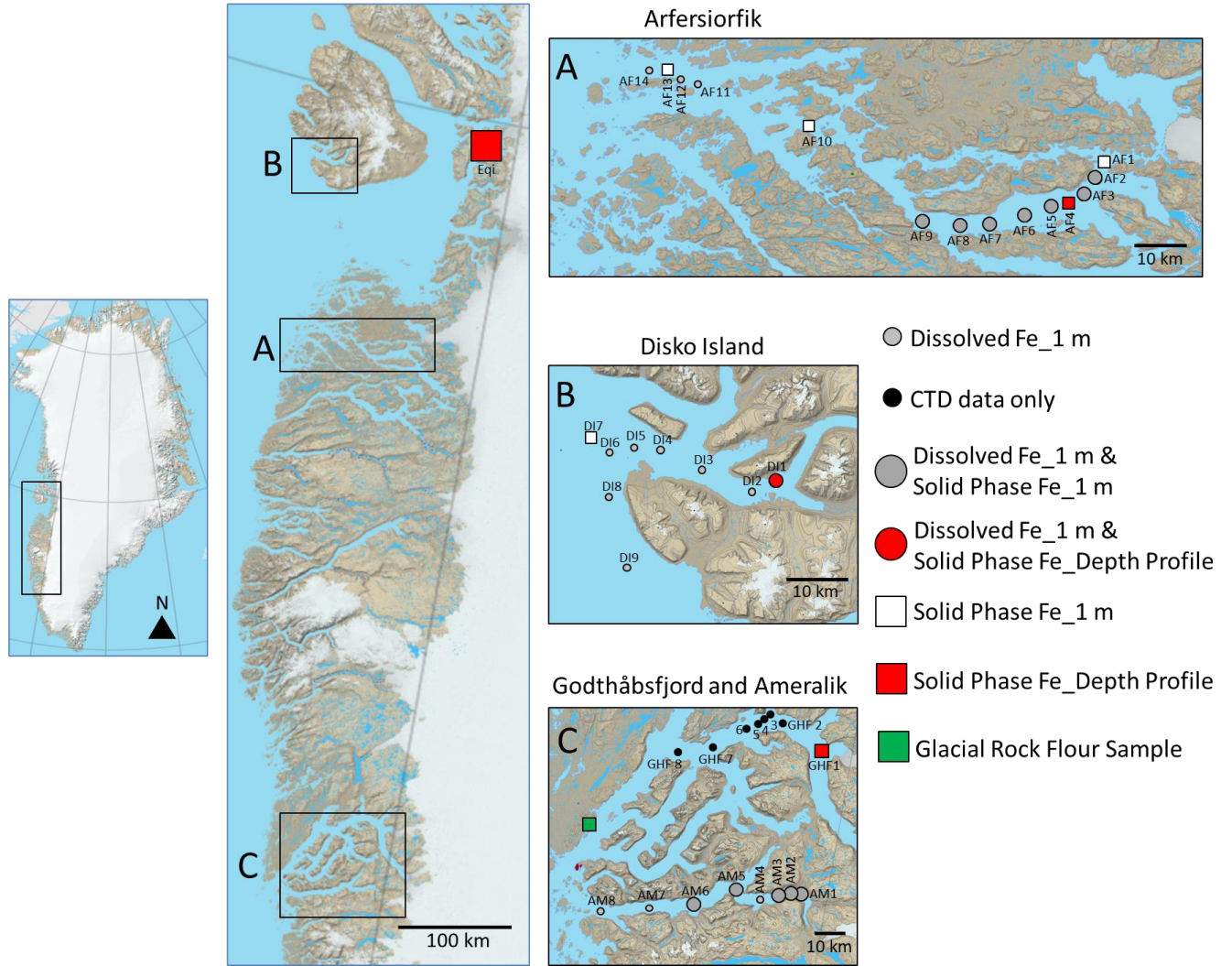
148
149   Figure 1: Map of Greenland showing the major transects of Disko Bay (A, B) and Ameralik
150   Fjord (C). The corresponding sampling locations and measurement types for the transects are
151   provided in the legend. The red square in the centre panel indicates Eqi Fjord where an
152   additional depth profile of solid-phase Fe speciation was measured. The green square indicates
153   where a rock flour sample was collected from a dry raised seabed. Maps were obtained from the
154   Geological Survey of Denmark and Greenland (GEUS) map database.

155

156   2.2 Sample collection and analysis

157   Fjord water was collected for measurements of dFe at ~1 m depth using a custom made

158   towfish device mounted on a winch ~2 m away from the ship's hull when underway (Disko Bay)

159   or from high density polyethylene (HDPE) bottles fitted to a HydroBios sampler on a nylon line

160   (Ameralik). The towfish was operated by continuously pumping water through tubing pre-

161   cleaned with 0.1 M HCl using a Teflon diaphragm pump. An inline filtration system (AcroPak

162   0.8/0.2 μm) was used to filter water samples. Water samples from Ameralik were filtered

163   through 0.2 μm Millipore syringe filters, which were flushed with 0.1 M HCl, ultrapure water

164   (18.2 MΩ cm MilliQ) and sample water before use. Filtered water was reserved in trace metal

165   clean 125 mL low density polyethylene (LDPE, Nalgene) bottles. The LDPE bottles were

166   prepared in advance using a three-stage washing procedure (1 day in detergent, 1 week in 2 M

167   HCl, 1 week in 2 M HNO_3 with three to five rinses of ultrapure water after each stage) and were

168   stored empty and double bagged until use. All filtered samples were acidified to pH <2.0 by the

169   addition of 180 μL HCl (UpA grade, Romil) and stored upright for at least 6 months prior to

170   analysis. Sample processing on board the ship was performed under a laminar flow hood. Fjord

171   water samples were pre-concentrated offline using a SEAFAST pre-concentration system exactly

172   as per Rapp et al., (2017) and analysed via ICP-MS at GEOMAR. The certified reference

173   materials NASS and CASS analysed alongside samples were in close agreement with certified

174   values (measured 6.09 ± 0.57 and 26.1±1.6; certified 6.29±0.47 and 27.93±2.1 nM, respectively).

175   Macronutrient samples were collected alongside dFe samples using the same sampling/filtration

176   equipment. Samples were then frozen and analysed after standing overnight at room temperature

177   in the dark for nitrate + nitrite, nitrite, phosphate and silicic acid concentrations using an auto-

178   analyser (Grasshoff et al., 1999). Detection limits were 0.09 μM NO_3, 0.06 μM PO_4 and 0.25 μM

179   silicic acid.

180   Where possible, fjord samples were collected in conjunction with measurements of

181   physical data, including salinity and temperature (i.e., CTD data), which was determined from ~1

182   m depth and is reported alongside dFe data. When/where CTD data were not collected in close

183   coordination with dFe sampling, a handheld LF 325 conductivity meter (WTW) was used to

184   record in situ temperature and salinity. The turbidity of surface waters and depth profiles of

185   select fjords was measured using a Seapoint turbidity sensor. In addition, turbidity in depth

186   profiles across a roughly 30 km transect of Godthåbsfjord (black symbols in Figure 1) was

187   collected with a laser in-situ scattering transmissometry (LISST) instrument (Sequoia Scientific).

188   Suspended sediment samples were obtained from select locations at discrete depths from

189   1 to 300 m using a 5 L Go-Flo bottle on a nylon line attached to a stainless-steel cable. A

190   vacuum pump with 0.2 µm polyethersulfone disk filters (25 mm diameter; Sartorius) was used to

191   filter the fjord water suspension aboard the ship immediately after sample collection. For each

192   depth and location, ~1-2 L of the suspension was filtered (or less if the filter clogged). The disk

193   filters with retained solids were then sealed in air-tight petri dishes while still wet and kept cold

194   throughout the cruise (stored in -80° C freezer) and during shipment to the home institute

195   (packed with dry ice).

196

197   2.3 Fe K-edge X-ray absorption spectroscopy

198   *2.3.1. Data collection and processing.*

199   Samples were analysed by Fe K-edge XAS at beam lines 2-2 and 4-1 of the Stanford

200   Synchrotron Radiation Lightsource (SSRL; Menlo Park, USA) and at the Balder beam line of the

201   MAX IV synchrotron (Lund, SE). Transmission and fluorescence data were recorded for each

202   sample at room temperature out to k of 12 to 13 Å^{-1}. The X-ray beam was calibrated to an Fe foil

203   (7112 eV) and second-order harmonics were avoided by detuning 20% (MAX IV) or 40-50%

204   (SSRL). Spectra were collected in quick-XAS mode at MAX IV, whereas standard data

205 acquisition parameters were used at SSRL. Individual scans for each sample were compared and

206 no beam damage was observed. Spectra were aligned, averaged and background-subtracted using

207 SixPack software (Webb, 2005) following standard methods described elsewhere (van

208 Genuchten et al., 2012). The extended X-ray absorption fine edge structure (EXAFS) spectra

209 were extracted using k^3-weighting and were Fourier-transformed over the k-range of 2 to 11 Å^{-1}

210 using a Kaiser-Bessel window with dk of 3 Å^{-1}. Further details on sample preparation and data

211 collection are given in the Supporting Information (SI).

212   In addition to Fe K-edge XAS data of experimental samples, we measured a suite of Fe

213 mineral reference spectra as part of the current study and in our previous work (van Genuchten et

214 al., 2019, 2014). Our study also includes Fe mineral reference spectra obtained from an online

215 database provided by Shoenfelt et al., (2017) and (2018), which was also collected at beam line

216 4-1 at SSRL, and received directly from the corresponding author of Yu et al., (2020), which was

217 collected at MAX IV.

218   *2.3.2. Fe K-edge XAS analysis.*

219   The Fe(II)/Fe$_{Tot}$ ratio of the solid samples was determined by X-ray absorption near edge

220 structure (XANES) analysis following the approach described in Shoenfelt et al., (2018). Briefly,

221 a calibration curve was generated using nine Fe-bearing reference minerals by plotting the edge

222 position, which is defined as the X-ray energy where the intensity of the normalized XANES

223 spectrum crosses 0.9 A, against the known Fe(II)/Fe$_{Tot}$ ratios of the reference minerals (Figure

224 S1 in the SI). The Fe(II)/Fe$_{Tot}$ ratio of the sediment samples was then calculated with the

225 calibration curve using the experimental edge energy. Uncertainty in the calculated Fe(II)/Fe$_{Tot}$

226 ratio was determined by regression analysis. We report uncertainty in the Fe(II)/Fe$_{Tot}$ ratios

227   determined with this method as the 95% confidence interval (CI). Additional details of this

228   XANES analysis are given in the SI.

229   The reference spectra used in the XANES analysis were also used to aid interpretations of

230   the experimental EXAFS spectra. This analysis was based on qualitative visual comparison of

231   characteristic fingerprints in the EXAFS spectra and Fourier transforms.

232   3. Results

233   3.1 Dissolved Fe

234   The dissolved Fe (dFe) concentration and salinity of fjord surface water (1 m depth) is

235   plotted from fjord head to mouth for each of the three transects in Figure 2. Measurements of dFe

236   from the Arfersiorfik transect, the longest transect performed in the Disko Bay region, varied

237   from 4.3 to 6.2 nM depending on sample location. This range of dFe values matches the range of

238   other dFe concentrations reported for glaciated fjords in Greenland (Hopwood et al., 2016;

239   Kanna et al., 2020). Compared to non-glaciated Arctic regions with similar salinities, these dFe

240   levels are similar to, or lower than riverine regions, which often exceed 10 nM (Dai and Martin,

241   1995; Guieu et al., 1996). The dFe in surface water of the Arfersiorfik transect was 5.7 nM in the

242   innermost sample location near the fjord head where the low salinity (13.6) indicated input of

243   fresh meltwater to the fjord. 10 km from the innermost sampling point of this transect, the dFe

244   reached a minimum of 4.3 nM (salinity of 14.5). The dFe increased to the greatest concentration

245   of 6.2 nM at the fjord mouth (salinity of 31.9), nearly 100 km from the initial sampling point.

246   When grouped by salinity, the dFe concentrations in Arfersiorfik surface waters were

247   significantly lower (4.7±0.6 nM) for sampling points with salinity <20 (i.e., those closer to the

248   fjord head) than for sampling points with salinity >20 (5.9±0.3 nM) (t-test, $p < 0.05$), though we

249   acknowledge the dFe levels in this fjord were relatively constant and all < 10 nM.

250   For the Disko Island transect, the dFe concentration in surface water ranged from 4.9 to

251   7.0 nM, slightly higher than the dFe measurements for the Arfersiorfik transect. In general, the

252   dFe measurements in the Disko Island transect were lower near the fjord head (4.9 to 5.6 nM)

253   where the salinity was lowest (2.8 to 19.9), and increased to the highest value of 7.0 nM near the

254   high-salinity (33.8 to 34.1) fjord mouth. Taking the average of all dFe measurements for Disko

255   Island gives 6.1±0.7 nM, indicating very similar dFe concentrations for the two transects around

256   Disko Bay.
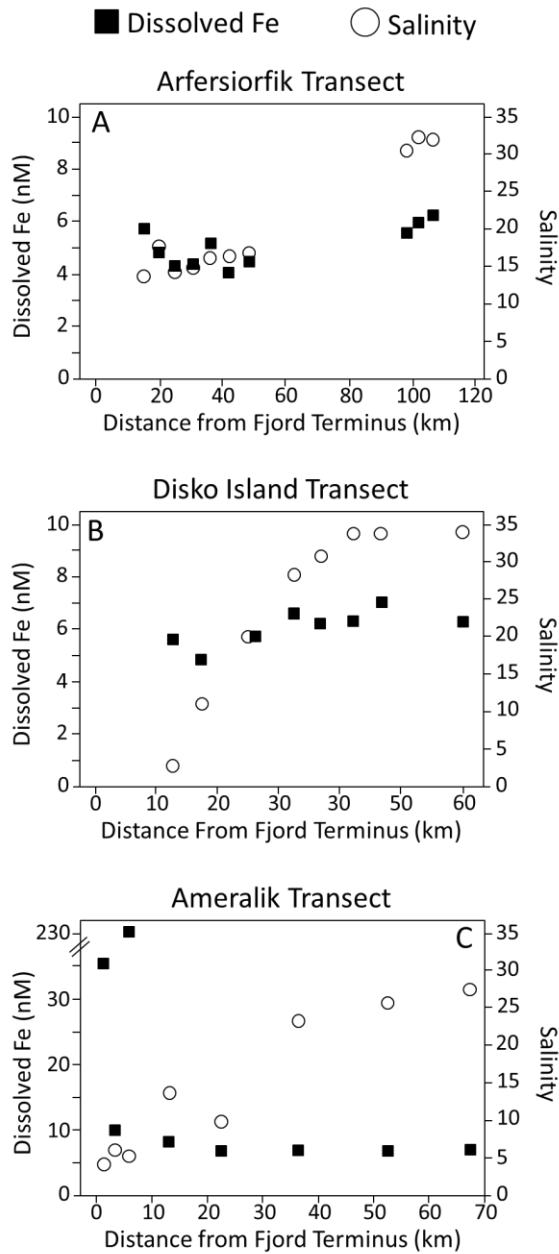
257
258
259   Figure 2: Dissolved Fe (dFe, filled squares) and salinity (open circles) along the three fjord
260   transects. The data are plotted as the distance away from the fjord terminus. Note the break in the
261   y-axis for the Ameralik transect.
262

263   The dFe measurements of Ameralik Fjord showed one key difference compared to those

264   of the two regions sampled in Disko Bay. In the area closest to the fjord head with the lowest

265   salinity (<7), the dFe of surface water reached up to 230 nM. The order of magnitude higher

266   surface water dFe near the innermost sampling location of the Ameralik transect compared to the

267   two Disko Bay transects is consistent with a continuous supply of dFe to the fjord head. It should

268   be noted however that this sampling location is considerably closer (~1 km away) to the main

269   glacier outflow than in any of the other systems sampled. As distance along the fjord increased, a

270   trend in decreasing dFe and increasing salinity was observed for Ameralik surface waters, but the

271   trend is much less evident when the samples <10 km from the fjord head are excluded. For

272   example, 11 km from the innermost sample location, a distance more comparable spatially to the

273   innermost samples from the Disko Bay region, the dFe concentration was 8.1 nM at a salinity of

274   13.7. At distances >35 km along the transect, the dFe and salinity were relatively stable, with the

275   lowest dFe concentration of 6.7 nM measured 51 km from the innermost sample location

276   (salinity of 25.8). The distinct decrease in dFe with increased salinity in the innermost area of

277   Ameralik Fjord agrees well with previous studies of glacially-modified fjords on similar spatial

278   scales (Hopwood et al., 2016; Schroth et al., 2014), which show sharp declines in dFe and

279   particulate Fe phases within a few km of the outflow into saline waters. In the fjords around

280   Disko Bay, such losses may have simply occurred closer to the glacier(s) than the first samples

281   were obtained.

282

283   3.2 Turbidity

284   Surface water turbidity varied significantly with salinity and distance along all fjords

285   (Figure 3). For the Arfersiorfik transect, the highest turbidity (>200 NTU) was measured in the

286   inner-fjord at 0-30 m depth, indicating the presence of a dense particle plume where the input of

287   fresh meltwater was largest. The turbidity decreased orders of magnitude with distance along

288   Arfersiorfik transect, particularly at distances >20 km, leading to the lowest turbidity of <1 NTU

289   measured furthest from the inner-fjord at 50 m depth. Similarly, turbidity in the Disko Island

290   transect decreased from >50 NTU to <1 NTU as the distance from the inner-fjord increased from

291   0 to >20 km (Figure 3). For Ameralik transect, the lens of turbid surface waters extended further

292   from the inner-fjord than for Arfersiorfik and Disko Island transects, with turbidity levels >10

293   NTU measured 30 km from the inner-fjord. It should be noted that a thin (~ 10 cm) surface layer

294   of extremely high turbidity was visually observed in inner Ameralik, which is not likely captured

295   in profile data. Nevertheless, the same trends in turbidity across the salinity gradient and with

296   depth were observed. Turbidity measurements for the 400 m depth profile (Figure S3) of

297   Godthåbsfjord (GHF 1 sample location) also indicated significant variation with depth as has

298   been noted at this site previously (Hopwood et al., 2018). Multiple spikes in turbidity were

299   observed, with the highest turbidity of 4.6 NTU measured near the surface (20-40 m), followed

300   by a less turbid spike near 240 m and another spike observed near the fjord bottom (400 m).

301   Turbidity measurements for surface waters along Godthåbsfjord revealed the highest turbidity

302   near the outflow of a large turbid lake (Lake Tasersuaq) at 0-20 m depth. The turbidity then

303   decreased substantially (>90% reduction) with increasing salinity, distance along the fjord and

304   depth.

305
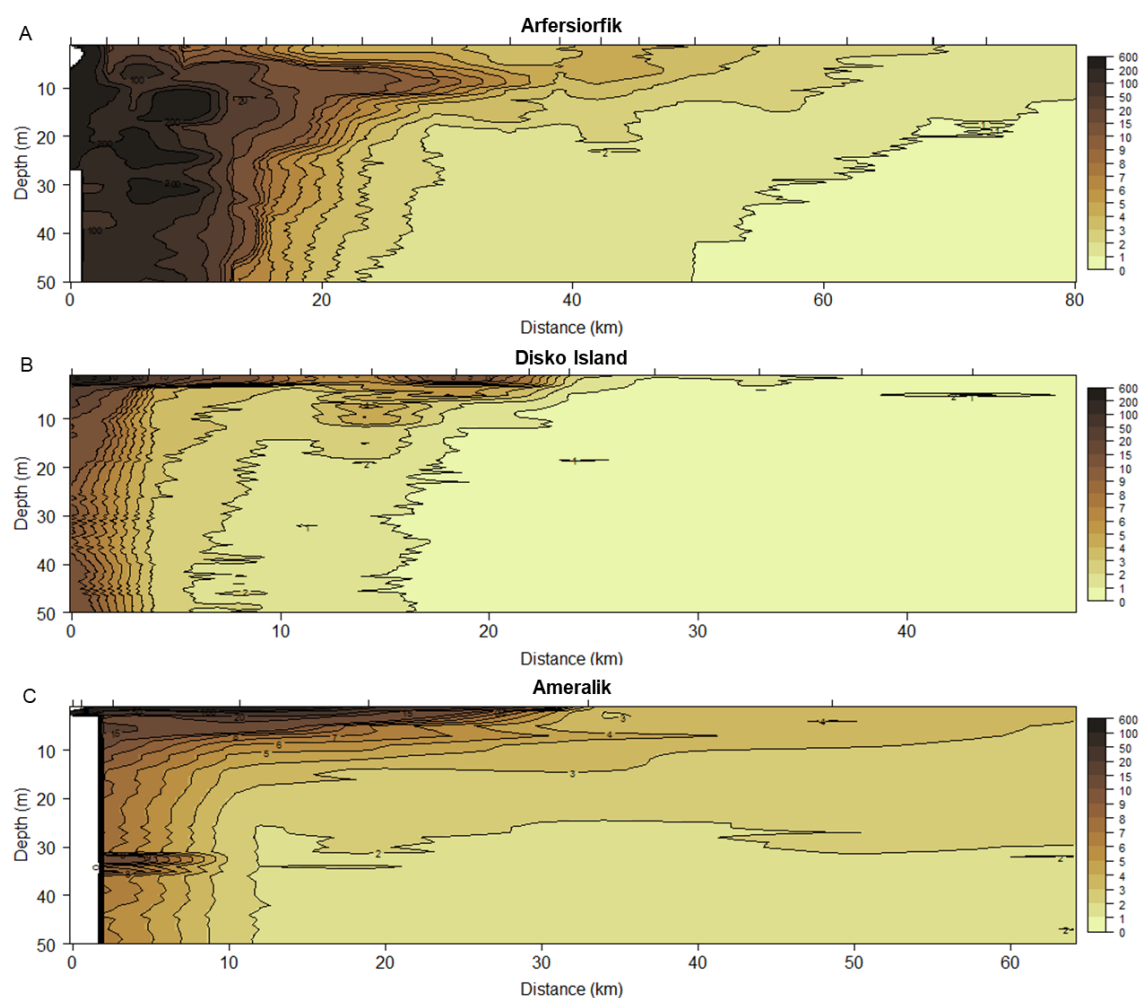
Figure 3: Turbidity (NTU) along Arfersiorfik (A), Disko Island (B) and Ameralik (C) transects.
The x-axis is given as distance from the sample location of inner-most fjord.

3.3 Fe K-edge XANES spectra of suspended sediments

3.3.1 Arfersiorfik *transect and Eqi Fjord.*

The Fe K-edge XANES spectra of sediment from the Arfersiorfik transect are compared
to the glacial rock flour sample and select Fe(II)- and Fe(III)-bearing reference minerals in
Figure 4. The Fe(II)/Fe$_{Tot}$ ratios of the samples calculated with the XANES edge energy are
listed in Table 1. Despite the nearly 100 km between suspended sediment collected near the
Arfersiorfik fjord head (AF 1) and mouth (AF 13; Figure 1) and the 100 m depth profile at the

17

317 AF 4 location, all samples displayed similar major XANES features. These prominent XANES

318 fingerprints include an absorption maximum near 7130.5 eV, two distinct shoulders before the

319 absorption maximum at 7122.6 and 7126.7 eV and a post-edge oscillation with a peak near

320 7143.3 eV. The shape of the XANES spectra of the Arfersiorfik suspended sediment also closely

321 reproduced the glacial rock flour sample (Figure 4B) and the reference spectrum of biotite, an

322 Fe(II)-bearing primary silicate. Although the sample spectra and biotite spectrum have some

323 small differences, particularly the slightly higher X-ray energy of the sample XANES edge

324 positions (Figure 4C), biotite matched the sample spectra far better than any other Fe(II) or

325 Fe(III) reference spectrum. For example, the olivine reference spectrum has a maximum near

326 7127.5 eV and lacks prominent shoulders at lower X-ray energies, whereas the XANES spectra

327 of the Fe(III)-bearing reference minerals are situated at higher X-ray energies.

328   The analysis of the XANES edge energy revealed a relatively narrow range of

329 Fe(II)/Fe$_{Tot}$ ratios of 0.79 to 0.86 for all Arfersiorfik samples (Table 1) regardless of depth and

330 fjord location, indicating the predominance of Fe(II) in these suspended particles. This

331 Fe(II)/Fe$_{Tot}$ range also matched the Fe(II) content of the glacial rock flour sample (0.81 ± 0.13).

332 Likewise, the depth profile of Eqi Fjord revealed suspended sediment containing high fractions

333 of Fe(II) (Table 1), which is consistent with the similar shape of the Eqi Fjord and Arfersiorfik

334 XANES spectra (Figure S2 in the SI). The calculated Fe(II)/Fe$_{Tot}$ ratios of all Eqi Fjord samples

335 ranged from 0.69 to 0.76 and were all within the fit-derived uncertainty (95% CI), indicating no

336 statistically significant difference in the average Fe(II) content of this depth profile. Collectively,

337 all Arfersiorfik and Eqi Fjord samples contained an Fe(II)/Fe$_{Tot}$ ratio of at least ~0.7, which is

338 significantly higher than the 30-40% Fe(II) determined by XANES analysis of glacial meltwater

339   sediments from Leverett Glacier and Kiattuut Sermiat (Greenland), but is comparable to the

340   range reported for Patagonian glacier outflows (Shoenfelt, 2019).

341
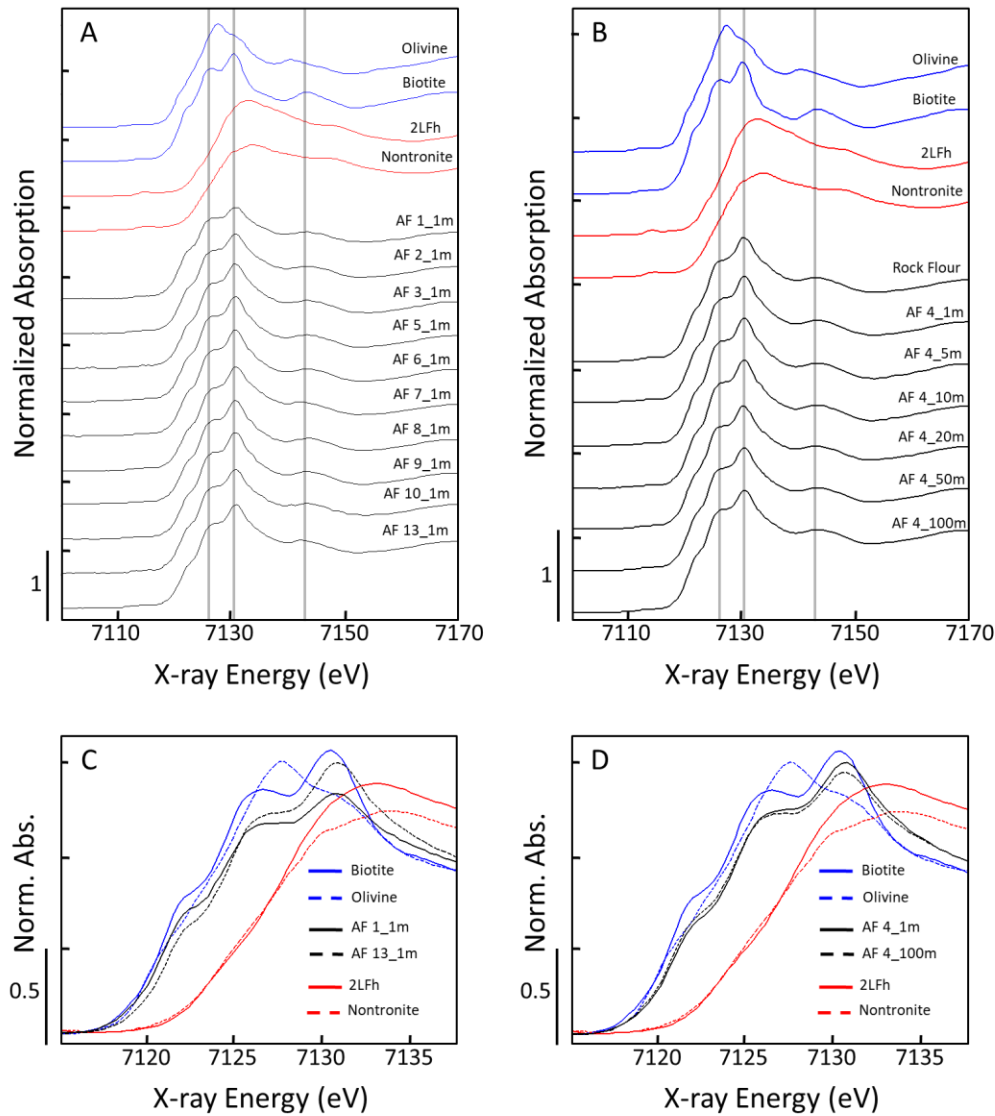
342
343   Figure 4. Comparison of the Fe K-edge XANES spectra of Fe(II)- and Fe(III)-bearing reference
344   minerals and glacially abraded rock flour (Rock Flour) with the XANES spectra of suspended
345   sediment from the Arfersiorfik (AF) transect. The sample spectra in panels A and B have been
346   offset by 0.5 A to facilitate comparison. The sample ID indicates the location and depth (e.g., AF
347   4_100m refers to the fourth sampling location of the Arfersiorfik transect at 100 m depth).

Table 1: Solid-phase Fe(II) Content Derived by XANES Analysis

	Sample	Fe(II)/Fe$_{Tot}$ (95% CI)		Sample	Fe(II)/Fe$_{Tot}$ (95% CI)
Arfersiorfik Transect	AF 1_1m	0.85 ± 0.09	**Disko Island Transect**	DI 1_1m	0.22 ± 0.08
	AF 2_1m	0.81 ± 0.10		DI 1_5m	0.27 ± 0.09
	AF 3_1m	0.79 ± 0.10		DI 1_10m	0.29 ± 0.09
	AF 4_1m	0.81 ± 0.09		DI 1_20m	0.29 ± 0.09
	AF 5_1m	0.81 ± 0.10		DI 1_50m	0.51 ± 0.09
	AF 6_1m	0.81 ± 0.10		DI 1_90m	0.38 ± 0.12
	AF 7_1m	0.79 ± 0.13		DI 7_1m	0.20 ± 0.10
	AF 9_1m	0.81 ± 0.10			
	AF 10_1m	0.85 ± 0.09	**Ameralik Transect & Godthåbsfjord**	AM 1_1m	0.84 ± 0.08
	AF 13_1m	0.81 ± 0.11		AM 2_1m	0.83 ± 0.08
				AM 3_1m	0.83 ± 0.08
	Rock Flour	0.81 ± 0.13		AM 5_1m	0.85 ± 0.08
	AF 4_1m	0.81 ± 0.09		AM 6_1m	0.85 ± 0.08
	AF 4_5m	0.81 ± 0.09		GHF_30m	0.90 ± 0.08
	AF 4_10m	0.83 ± 0.09		GHF_200m	0.87 ± 0.08
	AF 4_20m	0.86 ± 0.13		GHF_300m	0.85 ± 0.08
	AF 4_50m	0.84 ± 0.10			
	AF 4_100m	0.86 ± 0.10	**Eqi Fjord**	Eqi_1m	0.73 ± 0.09
				Eqi_7m	0.72 ± 0.10
				Eqi_10m	0.69 ± 0.10
				Eqi_20m	0.72 ± 0.10
				Eqi_30m	0.76 ± 0.10
				Eqi_40m	0.72 ± 0.10
				Eqi_50m	0.70 ± 0.10

349
350 The samples are grouped by their transect and depth. Sample IDs list the abbreviated location
351 and depth, with AF, DI, AM and GHF representing Arfersiorfik, Disko Island, Ameralik and
352 Godthåbsfjord, respectively. For example, AF 4_1m refers to the sample collected at the fourth
353 sampling location of the Arfersiorfik transect at 1 m depth (see Figure 1 for map), whereas
354 Eqi_10m refers to the Eqi Fjord depth profile at 10 m. The Rock Flour sample refers to the
355 glacially abraded rock flour collected from a raised seabed near Nuuk.

356

357 *3.3.2 Disko Island transect.*

358 Rather than displaying biotite-like absorption edge features, most of the Disko Island

359 transect samples had a relatively smooth XANES absorption edge with a maximum near 7133.3

360   eV, which more closely resembles the Fe(III)-rich reference minerals (Figure 5). Many samples

361   from Disko Island also exhibited a small shoulder near 7130 eV (indicated by * symbol in Figure

362   5) that is present in the reference spectrum of nontronite, an Fe(III)-bearing aluminosilicate

363   mineral. The post-edge oscillation of the Disko Island samples (maximum near 7147 eV) was a

364   closer match to nontronite and two-line ferrihydrite (2LFh), further supporting the predominance

365   of Fe(III). While most samples from this transect had similar XANES spectra, some deviation

366   was observed with depth, particularly at the innermost sample location (DI 1; see Figure 1 for

367   map). The XANES spectra of samples collected at depths from 1 to 20 m at this location

368   resembled the Fe(III) reference spectra, whereas the sediment at 50 m (and 90 m to a lesser

369   extent) displayed features consistent with at least a fraction of biotite, including the shift in the

370   absorption maximum to 7130.5 eV and the characteristic shoulder at 7126.7 eV (Figure 5). This

371   difference in Fe speciation with depth could indicate different water masses from coastal inflows

372   below 20 m depth in Disko Fjord. The XANES-derived $Fe(II)/Fe_{Tot}$ ratios confirmed the majority

373   of Fe(III) in the Disko Fjord samples, most of which contained <0.30 $Fe(II)/Fe_{Tot}$, with the

374   lowest $Fe(II)/Fe_{Tot}$ ratio of 0.20±0.13 obtained for sediments near the fjord mouth (DI 7) at 1 m

375   depth. However, the sediment collected from 50 m and 90 m depth at the fjord head contained

376      $Fe(II)/Fe_{Tot}$ ratios of 0.51±0.09 and 0.38±0.12, respectively.

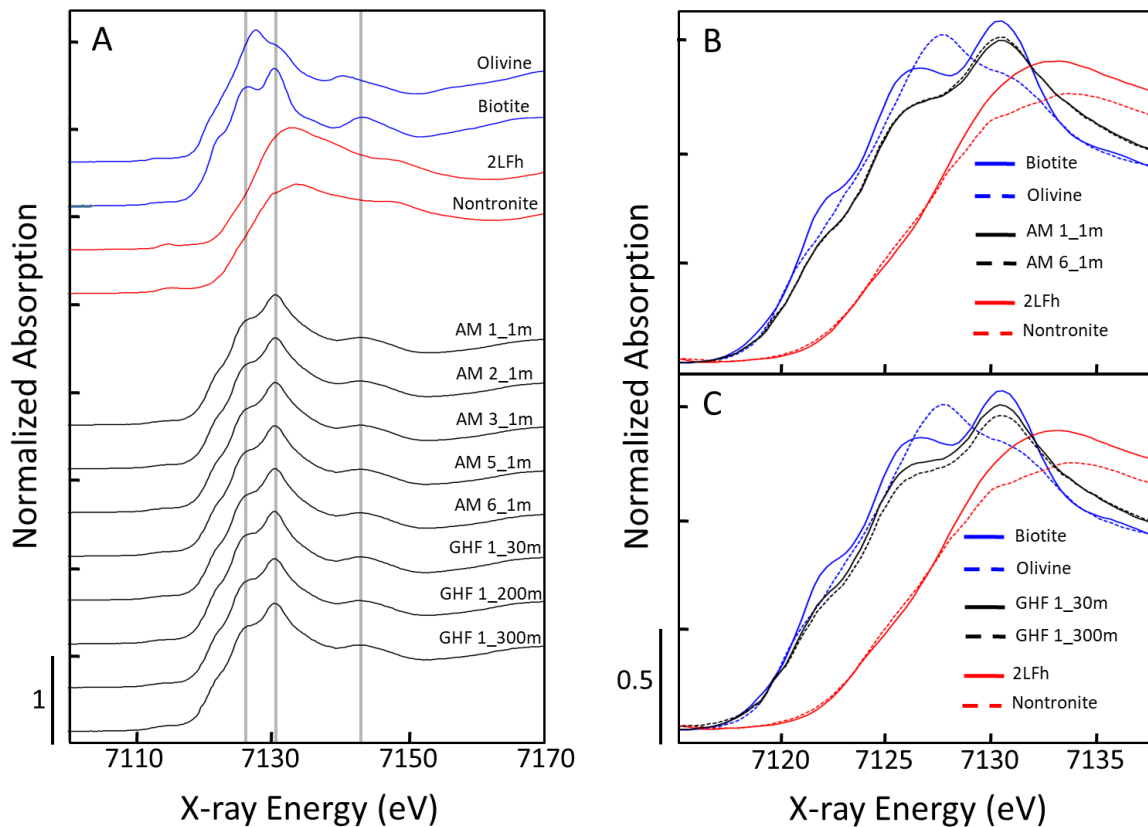377
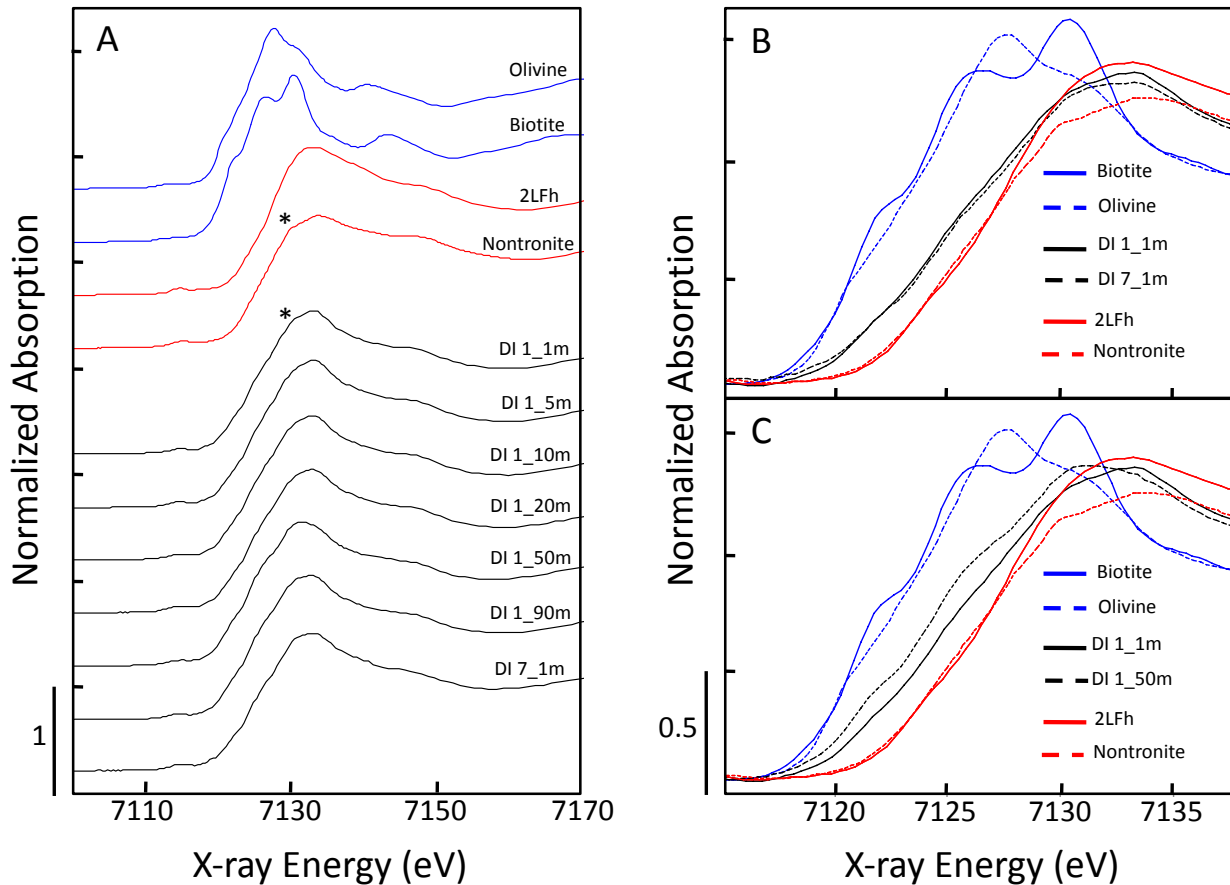
Figure 5. Comparison of the Fe K-edge XANES spectra of Fe(II)- and Fe(III)-bearing reference minerals with the XANES spectra of suspended sediment from the Disko Island (DI) transect. The sample spectra in panel A have been offset by 0.5 A to facilitate comparison. The sample ID indicates the location and depth (e.g., DI 1_1m refers to the first point of the Disko Island transect at 1 m).

3.3.3 Ameralik transect.

Very little variation in the XANES spectra of suspended sediment from the Ameralik

transect was observed (Figure 6). All samples displayed absorption maxima near 7130.5 eV, with

two distinct shoulders at 7122.6 and 7126.7 eV, consistent with biotite. In addition, the XANES

spectra of the suspended sediment depth profile taken from Godthåbsfjord, an adjacent fjord

system, also displayed the characteristic line shape and edge positions of biotite. Despite the

large distance separating Ameralik and Godthåbsfjord from the Arfersiorfik transect and Eqi

22

393   Fjord, the XANES spectra of all suspended sediment samples from these locations were similar,

394   suggesting Fe with an average biotite-like Fe(II) speciation is common in meltwater suspended

395   sediment in West Greenland. The Fe(II)/Fe$_{Tot}$ ratios for the Ameralik samples showed little

396   deviation with distance along the fjord, ranging from 0.83 to 0.85 (identical within fit-derived

397   uncertainty), which matches the Fe(II)/Fe$_{Tot}$ ratios of the Arfersiorfik samples. The

398   Godthåbsfjord depth profile produced the highest Fe(II)/Fe$_{Tot}$ ratios for any sample in our study,

399   reaching 0.90±0.08, though this value was not statistically different than the Ameralik samples

400   given the fit-derived uncertainty (95% CI).

401

402
403
404   Figure 6. Comparison of the Fe K-edge XANES spectra of Fe(II)- and Fe(III)-bearing reference
405   minerals with the XANES spectra of suspended sediment from the Ameralik (AM) transect and
406   Godthåbsfjord (GHF). The sample spectra in panel A have been offset by 0.5 A to facilitate
407   comparison.

408   3.4 Fe K-edge EXAFS spectra of end-member suspended sediment samples.

409   *3.4.1 EXAFS spectra of Fe(II)-rich samples.*

410   Because all suspended sediment samples with high $Fe(II)/Fe_{Tot}$ ratios had nearly identical

411   EXAFS spectra, we plot in Figure 7 only representative Fe(II)-rich end-member samples

412   containing >0.80 $Fe(II)/Fe_{Tot}$ collected from Disko Bay and Ameralik Fjord. The EXAFS

413   oscillations of the Fe(II)-rich suspended sediment and glacial rock flour samples had similar line

414   shape and phase. Key features in the EXAFS spectra for these samples include the slight

415   asymmetry of the first oscillation centred at 4 Å^{-1} (first * symbol in Figure 7), the low amplitude

416   beat feature at 5.2 Å^{-1} (second * symbol in Figure 7) and a double-peak with maxima near 7.5

417   and 8.1 Å^{-1} in the third oscillation (arrows in Figure 7). These characteristic EXAFS features

418   were also apparent in the biotite spectrum, but the features were more pronounced in biotite

419   (Figure 7B), especially the beat node at 5.2 Å^{-1} and the peak at 7.5 Å^{-1}. While biotite resembled

420   the samples better than many of the other Fe(II)-bearing references (i.e., siderite, olivine,

421   bentonite, hornblende and GR-SO4), the spectrum of Fe(II)-bearing chlorite was also a good

422   match. In particular, the chlorite EXAFS spectrum reproduced closely the amplitude of the

423   features at 5.2 and 7.5 Å^{-1}, but did not match the peak near 8.1 Å^{-1} better than biotite. The major

424   oscillation of the Fe(II)-chlorite spectrum at 6.0 Å^{-1} was also more asymmetric than the samples.

425   Differences between the EXAFS spectra of the samples and the Fe(II)-bearing reference

426   minerals are manifest in the Fourier transform (Figure 7C) primarily in the amplitude and

427   position of the second-shell peak. All Fe(II)-rich sediment samples exhibited an intense first-

428   shell Fe-O peak centred at 1.6 Å (R+ΔR) and a second-shell peak of moderate amplitude

429   positioned at 2.8 Å (R+ΔR). The position of the second-shell peak of the samples matched that

430   of biotite, but the biotite peak was considerably more intense, consistent with the higher

24

amplitude of the biotite EXAFS oscillations. The Fourier-transformed chlorite spectrum also

exhibited a second-shell peak that matched the position of the sediment samples, but the peak

intensity of chlorite was lower than the samples. The Fourier-transformed EXAFS spectra of

olivine and hornblende poorly reproduced the sample spectra, with the second-shell peak of

olivine located at a shorter interatomic distance than the samples and the second-shell peak of

hornblende having significantly lower amplitude. Therefore, in agreement with trends in key

features of the EXAFS spectra, the Fourier transforms suggest an average local Fe bonding

environment in the samples that lies intermediate between the Fe(II)-bearing primary silicates,
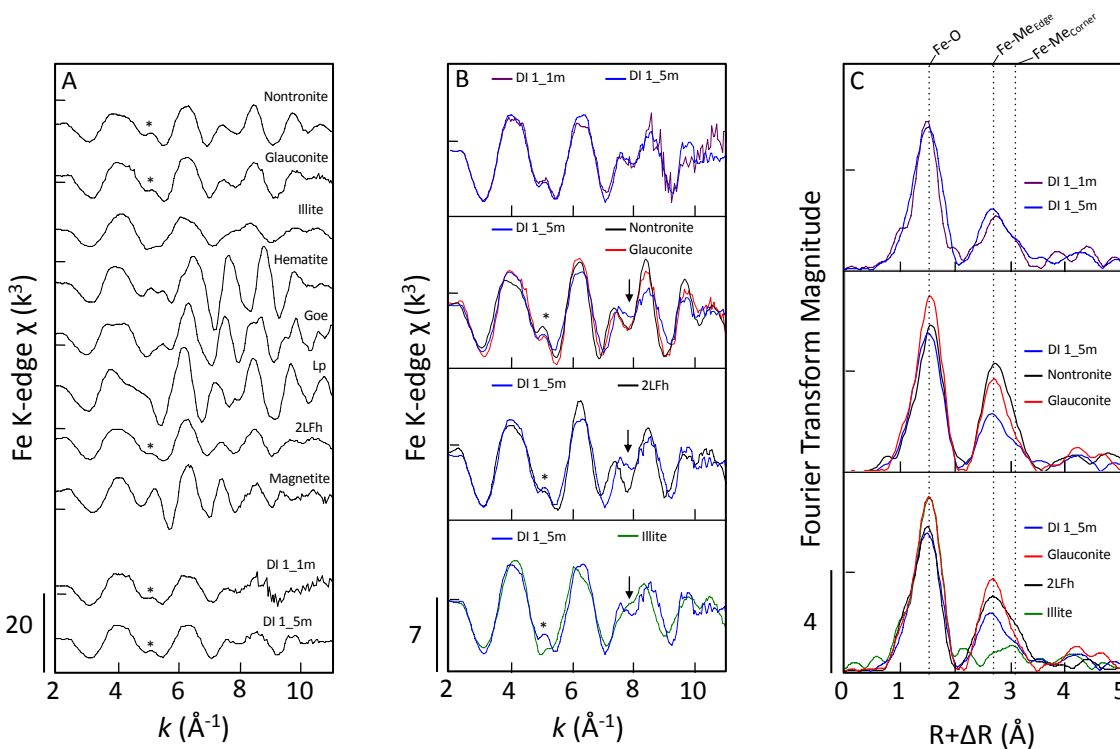
biotite and chlorite.
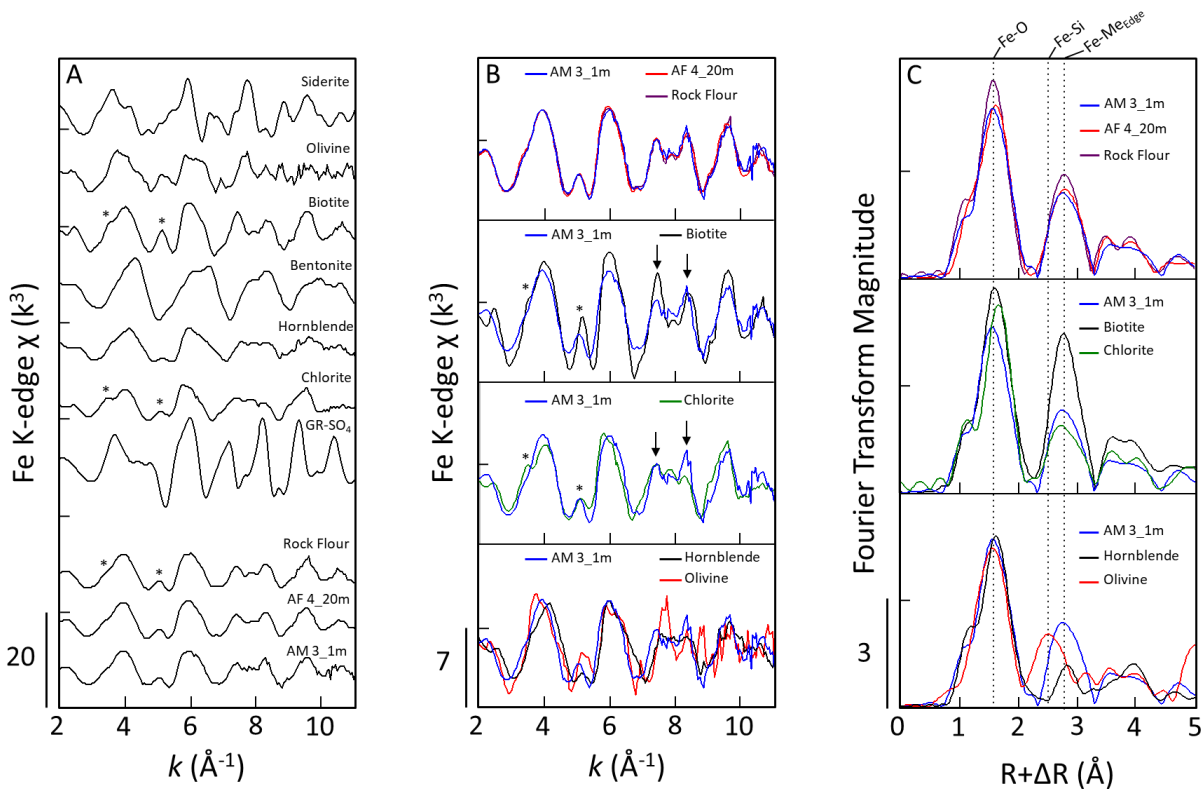
Figure 7: Fe K-edge EXAFS spectra (panels A and B) and corresponding Fourier transforms
(panel C) of Fe(II)-rich suspended sediment compared to spectra of Fe(II)-bearing reference
minerals. Sample spectra in panel A have been offset vertically by 10 Å^{-3} to facilitate
comparison, whereas spectra are overlain in B and C to highlight key differences between the
samples and reference minerals. The * symbol and arrows in A and B highlight fingerprint
regions of the EXAFS spectra.

447   *3.4.2 EXAFS spectra of Fe(III)-rich sediment.*

448   The EXAFS spectra of Fe(III)-rich end-member samples (i.e., those with $Fe(II)/Fe_{Tot}$

449   <0.30), which were only found in the Disko Island transect, are plotted alongside the EXAFS

450   spectra of a suite of Fe(III) reference minerals in Figure 8. Comparing the line shape and phase

451   of the EXAFS spectra in Figure 8, the closest matches to the samples include 2LFh, a poorly-

452   crystalline Fe(III) (oxyhydr)oxide, and the silicate minerals nontronite, glauconite and illite.

453   However, no single reference EXAFS spectrum reproduced perfectly all key features of the

454   samples. For example, the nontronite and glauconite EXAFS spectra overlapped with the first

455   oscillation of the samples at 4 $Å^{-1}$ and matched the small beat at 5.2 $Å^{-1}$ (* symbol in Figure 8),

456   but both reference minerals were not a good fit to the feature from 7.5 to 8 $Å^{-1}$ and both had

457   more intense oscillations at k >8 $Å^{-1}$ than the samples. The spectrum of 2LFh reproduced most of

458   the features of the samples, including the first oscillation, the beat feature at 5.2 $Å^{-1}$ and the

459   amplitude of the oscillations at k >8 $Å^{-1}$, but did not match the region from 7 to 8 $Å^{-1}$. Illite was

460   one of the only reference spectra that was a decent fit to the sample spectra at 7 to 8 $Å^{-1}$ (arrow in

461   Figure 8), but the illite spectrum did not reproduce the beat feature at 5.2 $Å^{-1}$.

462   The Fourier-transformed spectra in Figure 8C show that the difference between the

463   Fe(III)-bearing reference spectra and Fe(III)-rich samples is most pronounced in the second-shell

464   peak, which arises primarily from Fe-Fe and/or Fe-Si/Al/Mg backscattering. The position and

465   amplitude of the second-shell peak was nearly the same for the Fe(III)-rich end-member samples,

466   indicating similar average Fe bonding environments. However, the amplitude of the second-shell

467   peak for the samples was substantially lower than that of nontronite and glauconite and higher

468   than that of illite. While the second-shell peak exhibited a slight shoulder at higher R in the

469   samples, which is similar to the shoulder in the 2LFh peak arising from corner-sharing Fe-Fe

470   bonds, the amplitude of the samples was lower than that of 2LFh. The lower second-shell

471   amplitude of the Fe(III)-rich samples relative to 2LFh can be due to several reasons: 1) a lower

472   average crystallinity (i.e., less Fe-Fe bonding) of the host Fe phase compared to 2LFh, which has

473   a primary crystallite size of only 2.0 nm; 2) the presence of lighter atoms, such as Si, Mg and Al,

474   in the second coordination sphere, consistent with Fe(III)-rich aluminosilicates; or 3) the mixture

475   of poorly-ordered Fe(III) (oxyhydr)oxides and Fe(III)-rich silicates. Although we are unable to

476   distinguish unambiguously the average bonding environment of the Fe(III)-rich samples with our

477   data, key fingerprints in the XANES (* symbol in Figure 5) and EXAFS spectra are consistent

478   with a mixture of poorly-ordered Fe(III) (oxyhydr)oxides and Fe(III)-bearing silicates.

480   Figure 8: Fe K-edge EXAFS spectra (panels A and B) and corresponding Fourier transforms
481   (panel C) of Fe(III)-rich suspended sediment compared to spectra of Fe(III)-bearing reference
482   minerals. Sample spectra in panel A have been offset vertically by 13 Å^{-3} to facilitate
483   comparison. Goe, Lp and 2LFh represent goethite, lepidocrocite and two-line ferrihydrite,
484   respectively. The vertical dotted lines in C highlight peaks consistent with edge- and corner-
485   sharing Fe(III) polyhedra in 2LFh.

27

486   4. Discussion

487   4.1 Decoupling of dissolved and particulate Fe

488   Combining the measurements of dFe and solid-phase Fe speciation allows us to examine

489   the relationship between aqueous and particulate Fe. Previous studies propose that Fe(II)-rich

490   sediment is more bioaccessible than Fe(III)-rich sediment (Hawkings et al., 2018; Raiswell et al.,

491   2016) likely due to the higher solubility of Fe(II)-minerals and thus higher potential for dFe

492   release into solution. However, our dissolved and particulate Fe data do not support the

493   hypothesis that the predominance of Fe(II)-rich particles in glaciated fjords correlates with a

494   higher dFe concentration (Figure 9). Conversely, dFe seems remarkably insensitive to particulate

495   Fe speciation and we found no evidence that changes in dFe were related to the oxidation state of

496   solid-phase Fe. The decoupling of dissolved and particulate Fe was most pronounced when

497   comparing separate fjords. In the ~100 km Arfersiorfik transect, which was dominated by Fe(II)-

498   rich suspended sediment, the average dFe (5.1±0.8 nM) was similar to the average dFe (6.1±0.7

499   nM) in the Disko Fjord despite the suspended sediment consisting of Fe(III)-rich particles. This

500   inter-fjord comparison shows that the expected trend in dissolved and particulate Fe was actually

501   reversed (i.e., dFe was even slightly higher in meltwaters with Fe(III)-rich particles). Therefore,

502   our results suggest that the proposed higher bioavailability of Fe(II)-rich particles is not related

503   to a difference in dFe on this spatial scale. While we found that dFe levels in fjords dominated by

504   Fe(II)-rich sediment were not higher than those dominated by Fe(III)-rich sediment, our data are

505   not informative concerning the rate of dFe turnover. The small size of the dFe pool at low

506   salinities relative to the particulate Fe pool (dFe is rough 0.2-2% of total dissolvable Fe at inner-

507   fjord stations (Hopwood et al., 2016; Kanna et al., 2020)) means that even the well documented

508   transfer of dFe onto particle surfaces across the salinity gradient would not produce a significant

28

509 signal in the solid phase. In other words, while our fjord-scale dFe data are inconsistent with the

510 suspended particles serving as a net source of dFe within this environment, we cannot quantify

511 their role as a gross source. Soluble Fe(II) can be released from the biotite-like particles (Bray et

512 al., 2014), increasing dFe, but Fe(II) undergoes rapid oxidation and precipitation as Fe(III)

513 (oxyhydr)oxides, decreasing dFe. Any rapid production of dFe and transformation to particulate

514 Fe would be difficult to detect with bulk Fe K-edge XAS data considering its detection limits and

515 the much larger amount of Fe(II)-rich suspended particles in the fjords.

516   It should be noted that the investigated fjords are characterised as having a high

517 lithogenic influence (i.e., the particle loading is far higher than the offshore ocean). This means

518 Fe solubility may be saturated in solution such that the limits on dFe transfer between dissolved

519 and particulate phases are related to factors including the availability of dissolved organic

520 material to bind Fe and competition between these organics and particle surfaces as Fe binding

521 agents (Ardiningsih et al., 2020; Lippiatt et al., 2010). Conversely, in the surface offshore

522 environment, dFe is generally under-saturated and thus dFe concentrations could be more

523 sensitive to solid-phase Fe speciation. Furthermore, particles can affect Fe bioavailability to biota

524 via other mechanisms, with some evidence that direct contact with Fe(II)-rich solids increased Fe

525 availability to a model diatom *Phaeodactylum tricornutum*, although this subtlety mainly affects

526 how Fe availability is moderated in offshore Fe-deficient environments following dust deposition

527 (Shoenfelt et al., 2017).

528   An important implication of the observed dFe trends is that dFe concentrations are

529 relatively constant across strong turbidity gradients corresponding to the scale over which

530 sedimentation of most glacier derived particles occurs. This is also reflected in the Fe speciation

531 of raised marine deposits being similar to that of the freshly delivered glaciogenic suspended

532   sediments in the fjords, indicating no significant weathering of the particles during transport

533   from river outlet to settling at the fjord floor. Thus, the associated lateral fluxes of dFe are likely

534   independent of particulate Fe speciation and sediment load on this scale. If dFe concentration is

535   instead buffered at a relatively steady level in outflowing turbid near-surface waters, lateral

536   fluxes are expected to scale approximately with fjord turnover rates (Krisch et al., 2021), which

537   are poorly defined on a pan-Greenland scale. However, a non-linear response in dFe

538   concentrations to increasing meltwater input certainly remains possible because of the

539   confounding effect of increasing particle surface area on competition between particle surfaces

540   and dissolved organics for binding Fe (Ardiningsih et al., 2020).
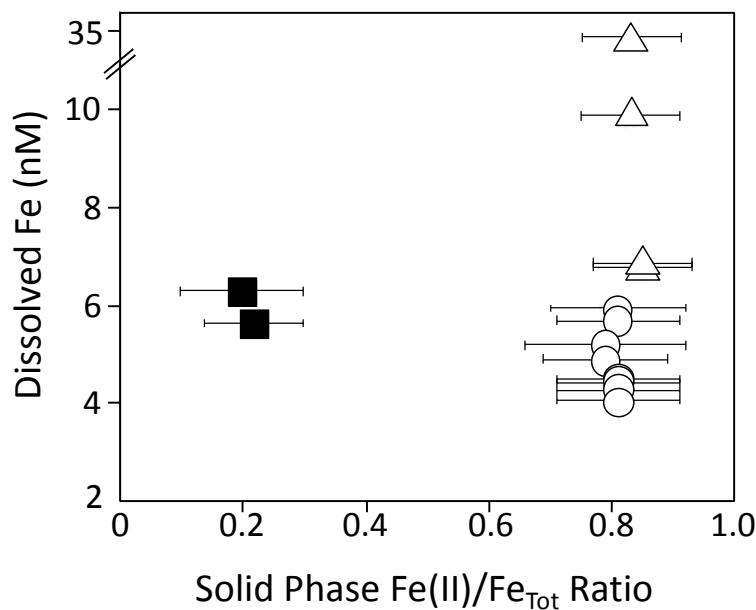
541

542   Figure 9: Dissolved Fe (dFe) plotted as a function of the XAS-derived solid-phase Fe(II)/Fe$_{Tot}$
543   ratio for suspended sediment samples collected from Arfersiorfik (open circles), Disko Island
544   (filled squares) and Ameralik (open triangles) transects. The data point from Ameralik transect
545   with >230 nm dFe (Fe(II)/Fe$_{Tot}$ ratio = 0.85) is not included. Note the break in the y-axis.
546

547   4.2 Importance of host Fe phase to persistence of Fe(II) in suspended fjord particles

548   While no clear relationship was evident between dFe concentrations and particulate Fe

549   speciation, solid-phase Fe speciation and the underlying bedrock geology do appear to be related.

550   The Fe(II)/Fe$_{Tot}$ ratio of suspended sediment groups by underlying Precambrian shield

551   (Arfersiorfik and Ameralik transects; open symbols in Figure 9) and tertiary basalts (Disko

552   Island transect; filled squares in Figure 9). This tight grouping of Fe(II)-rich silicates in

553   meltwater sourced from Precambrian shield and Fe(III)-rich particles from tertiary basalts might

554   be representative of many glacially-modified fjords around Greenland and can therefore be

555   helpful to predict the properties of particles transported into fjords. Furthermore, the data

556   indicate that the subglacial drainage basins for the studied meltwater systems along the coast of

557   mainland Greenland are dominated by similar felsic gneisses, and that tertiary basalt does not

558   constitute a significant proportion of the eroded basement.

559   In our study, all particulate Fe from meltwaters of Precambrian shield geology consisted

560   of 70-90% Fe(II), despite the hundreds of km between fjords, depth profiles extending to 300 m

561   and the expected long fjord mean residence time of the particles (water is present in the main

562   basin for 1-2 years in Godthåbsfjord (Mortensen et al., 2014)). Consistent with previous reports

563   of particles containing >70% Fe(II) from Alaskan ((Schroth et al., 2009)) and Patagonian

564   glaciers (Shoenfelt, 2019), our data indicated that suspended sediment near the West Greenland

565   coastline largely consists of Fe(II) fractions above 70%, which is substantially higher than the

566   ~40% Fe(II) detected previously in Greenlandic glacier sediments (Hawkings et al., 2018).

567   Furthermore, despite the fine grain size of these particles (Gunnarsen et al., 2019), which should

568   enhance particle reactivity, our data suggest that the majority of Fe in the suspended sediment

569   does not transform during fjord transport or particle settling. For example, the XAS data of

570   samples from the longest transects and deepest profiles in our study indicated similar Fe

571   speciation consistent with Fe(II) in a biotite-like coordination environment. This specific Fe(II)

572   bonding environment can help explain the persistence of solid-phase Fe(II), despite the lower

31

573   stability of Fe(II) than Fe(III) in oxic conditions. Biotite exchanges some cations readily,

574   particularly interlayer K^+, but the release of Fe(II) from crystalline biotite is expected to be

575   kinetically limited in conditions present in the fjords (i.e., pH > 7, low organic carbon

576   concentrations) (Bray et al., 2015, 2014). These observations are supported by the detection of

577   particles with similar speciation in core-top samples from the Greenland shelf, suggesting that

578   the fraction of particles advected laterally along fjords to the shelf is deposited without

579   significant processing (Shoenfelt, 2019). Although dFe produced from biotite dissolution is

580   expected to be minor, it could contribute to maintenance of the low dFe levels (i.e., <10 nM)

581   measured in most of the fjords. However, since dFe concentrations in the fjords are regulated by

582   a series of complex, co-occurring processes, such as fjord water mixing, biological uptake,

583   complexation by organic ligands, secondary mineral precipitation and sedimentation

584   (Ardiningsih et al., 2020; Lippiatt et al., 2010), it is not possible to accurately constrain gross

585   sources and sinks of dFe with our data.

586   The preservation of Fe(II) in glacial sediments has been attributed previously to

587   stabilization via an Fe(II)-amorphous silica nanoparticle aggregate (Hawkings et al., 2018).

588   However, the intense second-shell peak of the Fourier-transformed EXAFS spectra of the Fe(II)-

589   rich samples is inconsistent with the formation of an amorphous Fe(II)-silica particle. If Fe(II)

590   were hosted by a truly amorphous Si-rich material, the second-shell peak would have a

591   substantially lower amplitude or be absent altogether, as is common for Fe(II) in silicate glass

592   (Farges et al., 2005). Instead, the Fourier-transformed EXAFS data suggest an Fe(II) bonding

593   environment that is more ordered than Fe(II) in chlorite and less ordered than Fe(II) in biotite

594   (Figure 7). Therefore, the relatively rigid Fe(II) bonding environment of these particles and the

595   lack of evidence for Fe alteration in the suspended sediments suggest that the detection of Fe(II)

596   in these samples may not reflect enhanced Fe bioavailability or bioaccessibility in the water

597   column. Rather, it is likely that these particles require greater biogeochemical processing before

598   Fe becomes bioavailable, which could occur for settled particles in benthic environments (Laufer

599   et al., 2020), but does not appear to occur to any measurable extent in suspension on seasonal to

600   inter-annual timescales.

601

602   4.3 Can meltwater particle weathering be related to primary production in the studied regions?

603   In addition to the potential role of particles as a source of Fe, it is important to recognize

604   that meltwater runoff can also impact primary production via other mechanisms. The large turbid

605   plumes of particles near meltwater outflows (Figure 3) can attenuate light availability to

606   phytoplankton and can impair filter feeding organisms via particle ingestion (Murray et al.,

607   2015). Furthermore, while the raw glacially abraded rock flour has a minor phosphorous (P)

608   component (1.1 mg/g; Table S1) that could be a PO_4 source if released during weathering

609   (Gunnarsen et al., 2019), it is likely that the PO_4 fraction is contained in a separate apatite phase

610   that is more resistant to dissolution than biotite (Hawkings et al., 2016). Rather than a PO_4

611   source, biotite and other micas can be relatively effective at removing oxyanions from solution

612   via adsorption (Hartikainen and Hartikainen, 2008). The potential scavenging of PO_4 by

613   meltwater particles may also be the case for dissolved organic carbon (DOC), which can bind

614   effectively to biotite (Bray et al., 2015). All of the plumes surveyed had generally low PO_4 (and

615   low NO_3) concentrations (Table 2), but this likely reflects a combination of the low

616   macronutrient concentrations present in freshwater and nutrient uptake by primary producers

617   during spring and summer (Meire et al., 2017), rather than a singular effect of PO_4 sorption to

618   particles.

619 **Table 2: Composition of Surface Water Samples**
620

	Sample Location	Dist. Along Fjord (km)	Salinity	NO_3 (µM)	PO_4 (µM)	SiO_4 (µM)
Arfersiorfik Transect	AF 2	15.0	13.6	2.57	0.28	13.68
	AF 3	19.7	17.3	2.44	0.25	12.82
	AF 5	25.2	14.5	2.10	0.18	13.30
	AF 6	30.7	15.0	2.04	0.18	13.10
	AF 7	36.4	16.0	2.17	0.24	12.89
	AF 8	42.1	16.4	2.10	0.17	12.72
	AF 9	48.7	16.8	2.09	0.18	11.89
	AF 11	98.4	30.4	2.80	0.37	2.93
	AF 12	101.7	32.1	2.37	0.42	1.88
	AF 14	105.9	31.9	2.69	0.40	2.34
Disko Island Transect	DI 1	13.0	2.8	0.35	0.42	51.08
	DI 2	17.7	11.1	b/d	0.29	39.49
	DI 3	26.0	19.9	b/d	0.24	23.98
	DI 5	32.7	28.3	b/d	0.16	8.89
	DI 6	37.1	30.7	b/d	0.14	7.31
	DI 8	42.3	33.8	b/d	0.14	0.18
	DI 9	46.7	33.8	b/d	0.12	b/d
Ameralik Transect	AM 1	1.5	4.0	1.47	0.15	8.46
	AM 2	3.6	6.0	0.80	b/d	7.43
	AM 3	6.1	5.2	1.07	0.19	10.21
	AM 4	13.3	13.7	0.79	b/d	12.10
	AM 5	22.8	9.8	0.70	0.11	13.26
	AM 6	36.4	23.4	b/d	b/d	3.58
	AM 7	52.6	25.8	0.97	0.08	1.74
	AM 8	67.3	27.7	0.38	b/d	0.86

621 b/d indicates below the detection limit (0.09 µM for NO_3, 0.06 µM for PO_4 and 0.25 µM for SiO_4). A more detailed
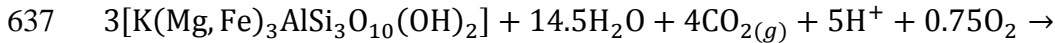622 version of this table is given in Table S2.
623
624   The XAS data suggested the widespread presence of Fe(II) in primary silicates, such as

625 biotite, which weathers following Eqn. 1 (Cleaves et al., 1970). Accordingly, one of the main

626 potential positive effects of meltwater particle weathering on primary production would be the

627 release of silicic acid, an essential nutrient for diatom growth. While the limited fjord surface

628 data presented herein restricts our ability to comment in detail on macronutrient budgets, we note

629 that all three inner-fjord environments show a large excess of silicic acid relative to nitrate

630 concentrations, with $Si(OH)_4$:NO_3 ratios consistently >5 across all regions with salinities <20

631 (Table 2). These ratios are in agreement with the excess of silicic acid relative to PO_4 and NO_3
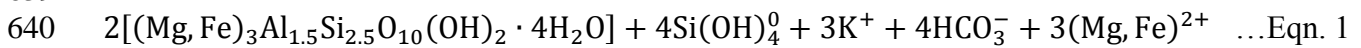
632   expected from concentrations in runoff around Greenland (Meire et al., 2016). The critical

633   difference between the release of dFe and silicic acid is that dFe is prone to scavenging, such that

634   a net release of silicic acid could be evident from weathering processes even if no net change in

635   dFe concentration was observed.

636

637    $3[K(Mg,Fe)_3AlSi_3O_{10}(OH)_2] + 14.5H_2O + 4CO_{2(g)} + 5H^+ + 0.75O_2 \rightarrow$
638   [Biotite]
639
640    $2[(Mg,Fe)_3Al_{1.5}Si_{2.5}O_{10}(OH)_2 \cdot 4H_2O] + 4Si(OH)_4^0 + 3K^+ + 4HCO_3^- + 3(Mg,Fe)^{2+}$ …Eqn. 1
641   [Vermiculite]
642

643   In summary, the relationship between meltwater particle weathering, nutrient availability

644   and primary production in the investigated fjords is complicated and depends partly on key

645   unknown factors, including the mineral weathering rates. The annual cycle of nutrient draw-

646   down and differences in bloom spatio-temporal dynamics due to light availability may also

647   confound attempts to interpret changes in macronutrient concentrations on this scale without

648   more extensive datasets.

649   5. Conclusions

650   We demonstrate that dFe was decoupled from solid-phase Fe speciation in suspended

651   sediment, with dFe showing little dependence on the particulate Fe oxidation state across three

652   glaciated fjords in West Greenland. Particulate Fe data were grouped by underlying bedrock

653   geology, with suspended sediment consisting of 70-90% biotite-like Fe(II) dominant in fjords

654   with Precambrian shield geology and poorly-ordered Fe(III) particles (<20-30% Fe(II)) derived

655   from tertiary basalts. Despite previous conjectures of more bioaccessible Fe in Fe(II)-rich

656   particles, our characterization data indicated no significant change in the average Fe oxidation

657   state and bonding environment of particles collected from individual fjord transects of up to 100

658   km, suggesting that Fe(II) in biotite-like coordination is not a labile form of Fe on this spatial

659   scale. Our results provide important constraints to predict the impact of meltwater outflows

660   containing Fe-rich particles on the biogeochemistry of glacially-modified water masses and

661   suggest that dFe on this spatial scale is buffered at a relatively constant low nM concentration

662   due to factors other than particle Fe mineralogy.

663

References

684 **References**

686 Adra, A., Morin, G., Ona-Nguema, G., Menguy, N., Maillot, F., Casiot, C., Bruneel, O., Lebrun, S., Juillot, F., Brest, J., 2013.
687   Arsenic scavenging by aluminum-substituted ferrihydrites in a circumneutral pH river impacted by acid mine drainage.
688   Env. Sci Technol 47, 12784–12792. https://doi.org/10.1021/es4020234

689 Ardiningsih, I., Krisch, S., Lodeiro, P., Reichart, G.-J., Achterberg, E.P., Gledhill, M., Middag, R., Gerringa, L.J.A., 2020.
690   Natural Fe-binding organic ligands in Fram Strait and over the northeast Greenland shelf. Mar. Chem. 224.
691   https://doi.org/10.1016/j.marchem.2020.103815

692 Bamber, J., van den Broeke, M., Ettema, J., Lenaerts, J., Rignot, E., 2018. Recent large increases in freshwater fluxes from
693   Greenland into the North Atlantic. Geophys. Res. Lett. 39, n/a-n/a. https://doi.org/10.1029/2012gl052552

694 Bhatia, M.P., Kujawinski, E.B., Das, S.B., Breier, C.F., Henderson, P.B., Charette, M.A., 2013. Greenland meltwater as a
695   significant and potentially bioavailable source of iron to the ocean. Nat. Geosci. 6, 274–278.
696   https://doi.org/10.1038/ngeo1746

697 Bray, A.W., Benning, L.G., Bonneville, S., Oelkers, E.H., 2014. Biotite surface chemistry as a function of aqueous fluid
698   composition. Geochim. Cosmochim. Acta 128, 58–70. https://doi.org/10.1016/j.gca.2013.12.002

699 Bray, A.W., Oelkers, E.H., Bonneville, S., Wolff-Boenisch, D., Potts, N.J., Fones, G., Benning, L.G., 2015. The effect of pH,
700   grain size, and organic ligands on biotite weathering rates. Geochim. Cosmochim. Acta 164, 127–145.
701   https://doi.org/10.1016/j.gca.2015.04.048

702 Carlson, L., Schwertmann, U., 1981. Natural ferrihydrites in surface deposits from Finalnd and their association with silica.
703   Geochim. Cosmochim. Acta 45, 421–429.

704 Cleaves, E.T., Godfrey, A.E., Bricker, O.P., 1970. Geochemical balance of a small watershed and its geomorphic implications.
705   Geol. Soc. Am. Bull. 81, 3015–3032.

706 Conway, T.M., Wolff, E.W., Rothlisberger, R., Mulvaney, R., Elderfield, H.E., 2015. Constraints on soluble aerosol iron flux to
707   the Southern Ocean at the Last Glacial Maximum. Nat Commun 6, 7850. https://doi.org/10.1038/ncomms8850

708 Dai, M.H., Martin, J.M., 1995. First data on trace metal level and behaviour in two major Arctic river-estuarine systems (Ob and
709   Yenisey) and in the adjacent Kara Sea, Russia. Earth Planet. Sci. Lett. 131, 127–141. https://doi.org/10.1016/0012-
710   821X(95)00021-4

711 Fan, S.-M., Moxim, W.J., Levy, H., 2006. Aeolian input of bioavailable iron to the ocean. Geophys. Res. Lett. 33.
712   https://doi.org/10.1029/2005gl024852

713 Farges, F., Rossano, S., Lefrere, Y., Wilke, M., Brown, G.E., 2005. Iron in silicate glasses: a systematic analysis of pre-edge,
714   XANES and EXAFS features. Phys. Scr. 115, 957–979.

715 Grasshoff, K., Kremling, K., Ehrhardt, M., 1999. Methods of seawater analysis. Wiley-VCH.

716 Guieu, C., Huang, W.W., Martin, J.M., Yong, Y.Y., 1996. Outflow of trace metals into the Laptev Sea by the Lena River. Mar.
717   Chem. 53, 255–267. https://doi.org/10.1016/0304-4203(95)00093-3

718 Gunnarsen, K.C., Jensen, L.S., Gomez-Munoz, B., Rosing, M.T., de Neergaard, A., 2019. Glacially abraded rock flour from
719   Greenland: Potenital for macronutrient supply to plants. J. Plant Nutr. Soil Sci. 182, 846–856.

720 Hartikainen, S.H., Hartikainen, H.H., 2008. Phosphorous retention by phlogopite-rich mine tailings. Appl. Geochemistry 23,
721   2716–2723.

722 Hawkings, J., Wadham, J., Tranter, M., Telling, J., Bagshaw, E., Beaton, A., Simmons, S.-L., Chandler, D., Tedstone, A.,
723   Nienow, P., 2016. The Greenland Ice Sheet as a hot spot of phosphorus weathering and export in the Arctic. Global
724   Biogeochem. Cycles 30, 191–210. https://doi.org/10.1002/2015gb005237

725 Hawkings, J.R., Benning, L.G., Raiswell, R., Kaulich, B., Araki, T., Abyaneh, M., Stockdale, A., Koch-Muller, M., Wadham,
726   J.L., Tranter, M., 2018. Biolabile ferrous iron bearing nanoparticles in glacial sediments. Earth Planet. Sci. Lett. 493, 92–
727   101.

728 Hawkings, J.R., Wadham, J.L., Tranter, M., Raiswell, R., Benning, L.G., Statham, P.J., Tedstone, A., Nienow, P., Lee, K.,
729   Telling, J., 2014. Ice sheets as a significant source of highly reactive nanoparticulate iron to the oceans. Nat Commun 5,
730   3929. https://doi.org/10.1038/ncomms4929

731 Hopwood, M.J., Carroll, D., Browning, T.J., Meire, L., Mortensen, J., Krisch, S., Achterberg, E.P., 2018. Non-linear response of
732   summertime marine productivity to increased meltwater discharge around Greenland. Nat Commun 9, 3256.
733   https://doi.org/10.1038/s41467-018-05488-8

734 Hopwood, M.J., Connelly, D.P., Arendt, K.E., Juul-Pedersen, T., Stinchcombe, M.C., Meire, L., Esposito, M., Krishna, R., 2016.
735   Seasonal changes in Fe along a glaciated Greenlandic fjord. Front. Earth Sci. 4, 1–13.
736   https://doi.org/https://doi.org/10.3389/feart.2016.00015

737 Kanna, N., Sugiyama, S., Fukamachi, Y., Nomura, D., Nishioka, J., 2020. Iron Supply by Subglacial Discharge Into a Fjord Near
738   the Front of a Marine- Terminating Glacier in Northwestern Greenland. Global Biogeochem. Cycles 34.
739   https://doi.org/10.1029/2020gb006567

740 Kelly, S.D., Hesterberg, D., Ravel, B., 2008. Analysis of soils and minerals using X-ray absorption spectroscopy. In Methods of
741   Soil Analysis. Part 5. Mineralogical Methods. SSA Book Series No.5. Soil Science Society of America.

742 Kraal, P., van Genuchten, C.M., Behrends, T., Rose, A.L., 2019. Sorption of phosphate and silicate alters dissolution kinetics of
743   poorly crystalline iron (oxyhydr)oxide. Chemosphere 234, 690–701. https://doi.org/10.1016/j.chemosphere.2019.06.071

744 Krisch, S., Hopwood, M.J., Schaffer, J., Al-Hashem, A., Höfer, J., Rutgers van der Loeff, M.M., Conway, T.M., Summers, B.A.,
745   Lodeiro, P., Ardiningsih, I., Steffens, T., Achterberg, E.P., 2021. The 79°N Glacier cavity modulates subglacial iron export

746   to the NE Greenland Shelf. Nat. Commun. 12. https://doi.org/10.1038/s41467-021-23093-0

747 Kuma, K., Matsunaga, K., 1995. Availability of colloidal ferric oxides to coastal marine phytoplankton. Mar. Biol. 122, 1–11.

748 Laufer, K., Michaud, A.B., Maisch, M., Byrne, J.M., Kappler, A., Patterson, M.O., Røy, H., Jørgensen, B.B., 2020. Bioavailable
749   iron produced through benthic cycling in glaciated Arctic fjords (Svalbard). Nat. Commun.

750 Lippiatt, S.M., Lohan, M.C., Bruland, K.W., 2010. The distribution of reactive iron in northern Gulf of Alaska coastal waters.
751   Mar. Chem. 121, 187–199. https://doi.org/10.1016/j.marchem.2010.04.007

752 Martin, J.H., Gordon, R.M., Fitzwater, S.E., 1991. The case for iron. Limnol. Oceanogr. 36, 1793–1802.

753 Mascarenhas, V.J., Zielinski, O., 2019. Hydrography-driven optical domains in the Vaigat-Disko Bay and Godthabsfjord: Effects
754   of glacial meltwater discharge. Front. Mar. Sci. 6, 1–19.

755 Matsunaga, K., Ohyama, T., Kuma, K., Kudo, I., Suzuki, Y., 1995. Photoreduction of manganese dioxide in seawater by organic
756   substances under ultraviolet or sunlight. Water Res. 29, 757–759. https://doi.org/10.1016/0043-1354(94)00190-I

757 Meire, L., Meire, P., Struyf, E., Krawczyk, D.W., Arendt, K.E., Yde, J.C., Juul Pedersen, T., Hopwood, M.J., Rysgaard, S.,
758   Meysman, F.J.R., 2016. High export of dissolved silica from the Greenland Ice Sheet. Geophys. Res. Lett. 43, 9173–9182.
759   https://doi.org/10.1002/2016gl070191

760 Meire, L., Mortensen, J., Meire, P., Juul-Pedersen, T., Sejr, M.K., Rysgaard, S., Nygaard, R., Huybrechts, P., Meysman, F.J.R.,
761   2017. Marine-terminating glaciers sustain high productivity in Greenland fjords. Glob. Chang. Biol. 00, 1–14.

762 Mortensen, J., Bendtsen, J., Lennert, K., Rysgaard, S., 2014. Seasonal variability of the circulation system in a west Greenland
763   tidewater outlet glacier fjord, Godthåbsfjord (64°N). J. Geophys. Res. Earth Surf. 119, 2591–2603.
764   https://doi.org/10.1002/2014JF003267

765 Murray, C., Markager, S., Stedmon, C.A., Juul Pedersen, T., Sejr, M.K., Bruhn, A.N.V.-B., 2015. The influence of glacial melt
766   water on bio-optical properties in two contrastig Greenlandic fjords. Estuar. Coast. Shelf Sci. 163, 72–83.

767 Naeraa, T., Kemp, A.I.S., Schersten, A., Rehnstrom, E., Rosing, M.T., Whitehouse, M.J., 2014. A lower crustal mafic source for
768   the ca. 2550 Ma Qorqut Granite Complex in southern West Greenland. Lithos 192, 291–304.

769 Raiswell, R., 2011. Iceberg-hosted nanoparticulate Fe in the Southern Ocean: Mineralogy, origin, dissolution kinetics and source
770   of bioavailable Fe. Deep Sea Res. Part II Top. Stud. Oceanogr. 58, 1364–1375. https://doi.org/10.1016/j.dsr2.2010.11.011

771 Raiswell, R., Hawkings, J.R., Benning, L.G., Baker, A.R., Death, R., Albani, S., Mahowald, N., Krom, M.D., Poulton, S.W.,
772   Wadham, J., Tranter, M., 2016. Potentially bioavailable iron delivery by iceberg-hosted sediments and atmospheric dust to
773   the polar oceans. Biogeosciences 13, 3887–3900. https://doi.org/10.5194/bg-13-3887-2016

774 Raiswell, R., Tranter, M., Benning, L.G., Siegert, M., De'ath, R., Huybrechts, P., Payne, T., 2006. Contributions from glacially
775   derived sediment to the global iron (oxyhydr)oxide cycle: Implications for iron delivery to the oceans. Geochim.
776   Cosmochim. Acta 70, 2765–2780. https://doi.org/10.1016/j.gca.2005.12.027

777 Raiswell, R., Vu, H.P., Brinza, L., Benning, L.G., 2010. The determination of labile Fe in ferrihydrite by ascorbic acid extraction:
778   Methodology, dissolution kinetics and loss of solubility with age and de-wartering. Chem. Geol. 278, 70–79.

779 Rapp, I., Schlosser, C., Rusiecka, D., Gledhill, M., Achterberg, E.P., 2017. Automated preconcentration of Fe, Zn, Cu, Ni, Cd,
780   Pb, Co, and Mn in seawater with analysis using high-resolution sector field inductively-coupled plasma mass
781   spectrometry. Anal. Chim. Acta 976, 1–13. https://doi.org/10.1016/j.aca.2017.05.008

782 Schlitzer, R., Anderson, R.F., Dodas, E.M., Lohan, M., Geibert, W., Tagliabue, A., Bowie, A., Jeandel, C., Maldonado, M.T.,
783   Landing, W.M., Cockwell, D., Abadie, C., Abouchami, W., Achterberg, E.P., Agather, A., Aguliar-Islas, A., van Aken,
784   H.M., Andersen, M., Archer, C., Auro, M., de Baar, H.J., Baars, O., Baker, A.R., Bakker, K., Basak, C., Baskaran, M.,
785   Bates, N.R., Bauch, D., van Beek, P., Behrens, M.K., Black, E., Bluhm, K., Bopp, L., Bouman, H., Bowman, K., Bown, J.,
786   Boyd, P., Boye, M., Boyle, E.A., Branellec, P., Bridgestock, L., Brissebrat, G., Browning, T., Bruland, K.W., Brumsack,
787   H.-J., Brzezinski, M., Buck, C.S., Buck, K.N., Buesseler, K., Bull, A., Butler, E., Cai, P., Mor, P.C., Cardinal, D., Carlson,
788   C., Carrasco, G., Casacuberta, N., Casciotti, K.L., Castrillejo, M., Chamizo, E., Chance, R., Charette, M.A., Chaves, J.E.,
789   Cheng, H., Chever, F., Christl, M., Church, T.M., Closset, I., Colman, A., Conway, T.M., Cossa, D., Croot, P., Cullen,
790   J.T., Cutter, G.A., Daniels, C., Dehairs, F., Deng, F., Dieu, H.T., Duggan, B., Dulaquais, G., Dumousseaud, C.,
791   Echegoyen-Sanz, Y., Edwards, R.L., Ellwood, M., Fahrbach, E., Fitzsimmons, J.N., Russell Flegal, A., Fleisher, M.Q., van
792   de Flierdt, T., Frank, M., Friedrich, J., Fripiat, F., Fröllje, H., Galer, S.J.G., Gamo, T., Ganeshram, R.S., Garcia-Orellana,
793   J., Garcia-Solsona, E., Gault-Ringold, M., George, E., Gerringa, L.J.A., Gilbert, M., Godoy, J.M., Goldstein, S.L.,
794   Gonzalez, S.R., Grissom, K., Hammerschmidt, C., Hartman, A., Hassler, C.S., Hathorne, E.C., Hatta, M., Hawco, N.,
795   Hayes, C.T., Heimbürger, L.-E., Helgoe, J., Heller, M., Henderson, G.M., Henderson, P.B., van Heuven, S., Ho, P.,
796   Horner, T.J., Hsieh, Y.-T., Huang, K.-F., Humphreys, M.P., Isshiki, K., Jacquot, J.E., Janssen, D.J., Jenkins, W.J., John,
797   S., Jones, E.M., Jones, J.L., Kadko, D.C., Kayser, R., Kenna, T.C., Khondoker, R., Kim, T., Kipp, L., Klar, J.K., Klunder,
798   M., Kretschmer, S., Kumamoto, Y., Laan, P., Labatut, M., Lacan, F., Lam, P.J., Lambelet, M., Lamborg, C.H., Le Moigne,
799   F.A.C., Le Roy, E., Lechtenfeld, O.J., Lee, J.-M., Lherminier, P., Little, S., López-Lora, M., Lu, Y., Masque, P., Mawji,
800   E., McClain, C.R., Measures, C., Mehic, S., Barraqueta, J.-L.M., van der Merwe, P., Middag, R., Mieruch, S., Milne, A.,
801   Minami, T., Moffett, J.W., Moncoiffe, G., Moore, W.S., Morris, P.J., Morton, P.L., Nakaguchi, Y., Nakayama, N.,
802   Niedermiller, J., Nishioka, J., Nishiuchi, A., Noble, A., Obata, H., Ober, S., Ohnemus, D.C., van Ooijen, J., O'Sullivan, J.,
803   Owens, S., Pahnke, K., Paul, M., Pavia, F., Pena, L.D., Peters, B., Planchon, F., Planquette, H., Pradoux, C., Puigcorbé, V.,
804   Quay, P., Queroue, F., Radic, A., Rauschenberg, S., Rehkämper, M., Rember, R., Remenyi, T., Resing, J.A., Rickli, J.,
805   Rigaud, S., Rijkenberg, M.J.A., Rintoul, S., Robinson, L.F., Roca-Martí, M., Rodellas, V., Roeske, T., Rolison, J.M.,
806   Rosenberg, M., Roshan, S., Rutgers van der Loeff, M.M., Ryabenko, E., Saito, M.A., Salt, L.A., Sanial, V., Sarthou, G.,
807   Schallenberg, C., Schauer, U., Scher, H., Schlosser, C., Schnetger, B., Scott, P., Sedwick, P.N., Semiletov, I., Shelley, R.,

808   Sherrell, R.M., Shiller, A.M., Sigman, D.M., Singh, S.K., Slagter, H.A., Slater, E., Smethie, W.M., Snaith, H., Sohrin, Y.,
809   Sohst, B., Sonke, J.E., Speich, S., Steinfeldt, R., Stewart, G., Stichel, T., Stirling, C.H., Stutsman, J., Swarr, G.J., Swift,
810   J.H., Thomas, A., Thorne, K., Till, C.P., Till, R., Townsend, A.T., Townsend, E., Tuerena, R., Twining, B.S., Vance, D.,
811   Velazquez, S., Venchiarutti, C., Villa-Alfageme, M., Vivancos, S.M., Voelker, A.H.L., Wake, B., Warner, M.J., Watson,
812   R., van Weerlee, E., Alexandra Weigand, M., Weinstein, Y., Weiss, D., Wisotzki, A., Woodward, E.M.S., Wu, J., Wu, Y.,
813   Wuttig, K., Wyatt, N., Xiang, Y., Xie, R.C., Xue, Z., Yoshikawa, H., Zhang, J., Zhang, P., Zhao, Y., Zheng, L., Zheng, X.-
814   Y., Zieringer, M., Zimmer, L.A., Ziveri, P., Zunino, P., Zurbrick, C., 2018. The GEOTRACES Intermediate Data Product
815   2017. Chem. Geol. 493, 210–223. https://doi.org/10.1016/j.chemgeo.2018.05.040
816 Schroth, A.W., Crusius, J., Hoyer, I., Campbell, R., 2014. Estuarine removal of glacial iron and implications for iron fluxes to the
817   ocean. Geophys. Res. Lett. 41, 3951–3958. https://doi.org/10.1002/2014gl060199
818 Schroth, A.W., Crusius, J., Sholkovitz, E.R., Bostick, B.C., 2009. Iron solubility driven by speciation in dust sources to the
819   ocean. Nat. Geosci. 2, 337–340. https://doi.org/10.1038/ngeo501
820 Shoenfelt, E.M., 2019. Interactions between glacial activity, dust-borne iron speciation, diatom productivity, and the biological
821   pump. Earth Environ. Sci. Columbia University.
822 Shoenfelt, E.M., Sun, J., Winckler, G., Kaplan, M.R., Borunda, A.L., Farrell, K.R., Moreno, P.I., Gaiero, D.M., Recasens, C.,
823   Sambrotto, R.N., Bostick, B.C., 2017. High particulate iron(II) content in glacially sourced dusts enhances productivity of
824   a model diatom. Sci Adv 3, e1700314. https://doi.org/10.1126/sciadv.1700314
825 Shoenfelt, E.M., Winckler, G., Lamy, F., Anderson, R.F., Bostick, B.C., 2018. Highly bioavailable dust-borne iron delivered to
826   the Southern Ocean during glacial periods. Proc Natl Acad Sci U S A 115, 11180–11185.
827   https://doi.org/10.1073/pnas.1809755115
828 Statham, P.J., Skidmore, M., Tranter, M., 2008. Inputs of glacially derived dissolved and colloidal iron to the coastal ocean and
829   implications for primary productivity. Global Biogeochem. Cycles 22, n/a-n/a. https://doi.org/10.1029/2007gb003106
830 Sukstorf, F.N., Bennike, O., Elberling, B., 2020. Glacial Rock Flour as Soil Amendment in Subarctic Farming in South
831   Greenland. Land 9. https://doi.org/10.3390/land9060198
832 Tagliabue, A., Bowie, A.R., Boyd, P.W., Buck, K.N., Johnson, K.S., Saito, M.A., 2017. The integral role of iron in ocean
833   biogeochemistry. Nature 543, 51–59. https://doi.org/10.1038/nature21058
834 van Genuchten, C.M., Addy, S.E.A., Pena, J., Gadgil, A.J., 2012. Removing arsenic from synthetic groundwater with iron
835   electrocoagulation: An Fe and As K-edge EXAFS study. Environ. Sci. Technol. 46, 986–994.
836   https://doi.org/10.1021/es201913a
837 van Genuchten, C.M., Behrends, T., Dideriksen, K., 2019. Emerging investigator series: interdependency of green rust
838   transformation and the partitioning and binding mode of arsenic. Env. Sci Process Impacts 21, 1459–1476.
839   https://doi.org/10.1039/c9em00267g
840 van Genuchten, C.M., Pena, J., Amrose, S.E., Gadgil, A.J., 2014. Structure of Fe(III) precipitates generated by the electrolytic
841   dissolution of Fe(0) in the presence of groundwater ions. Geochim. Cosmochim. Acta 127, 285–304.
842 Vizcaíno, M., Lipscomb, W.H., Sacks, W.J., van den Broeke, M., 2014. Greenland Surface Mass Balance as Simulated by the
843   Community Earth System Model. Part II: Twenty-First-Century Changes. J. Clim. 27, 215–226.
844   https://doi.org/10.1175/jcli-d-12-00588.1
845 Von Der Heyden, B.P., Roychoudhury, A.N., Mtshali, T.N., Tyliszczak, T., Myneni, S.C.B., 2012. Chemically and
846   geographically distinct solid-phase iron pools in the Southern Ocean. Science (80-.). 338, 1199–1201.
847   https://doi.org/10.1126/science.1227504
848 Webb, S., 2005. SIXPACK: a graphical user interface for XAS analysis using IFEFFIT. Phys. Scr. T115, 1011–1014.
849 Yu, C., Drake, H., Dideriksen, K., Tillberg, M., Song, Z., Mørup, S., Åström, M.E., 2020. A Combined X-ray Absorption and
850   Mössbauer Spectroscopy Study on Fe Valence and Secondary Mineralogy in Granitoid Fracture Networks: Implications
851   for Geological Disposal of Spent Nuclear Fuels. Environ. Sci. Technol. 54, 2832–2842.
852   https://doi.org/10.1021/acs.est.9b07064
853

Click here to access/download
Supplementary material for online publication only
Supporting Document_Fe
speciation_Revised_Final.docx